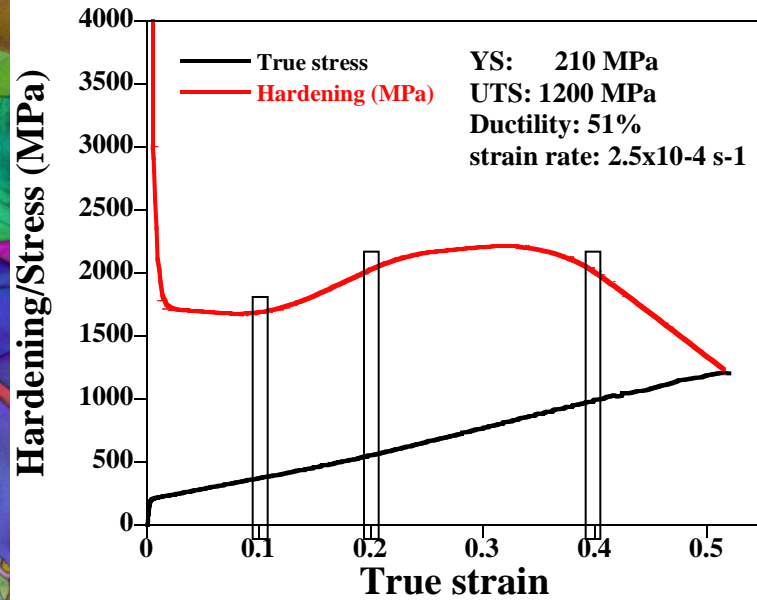
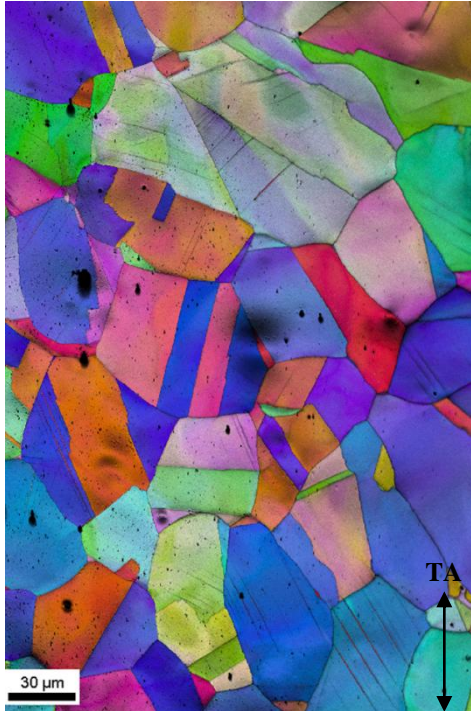


Fe-22Mn-0.6C (wt%) TWIP steel

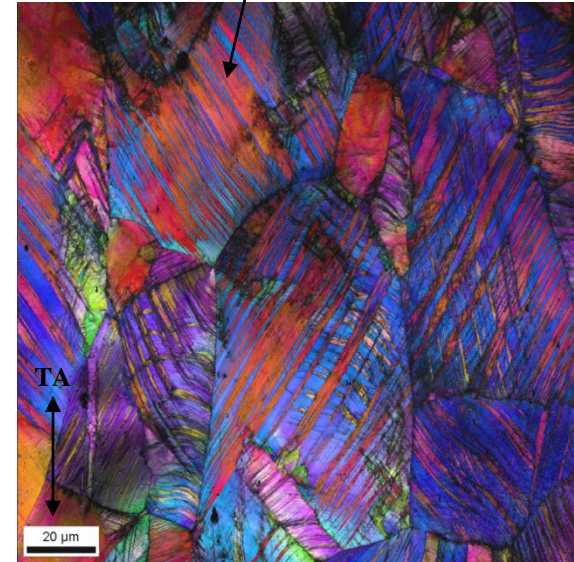
Tensile test at room temperature

10%

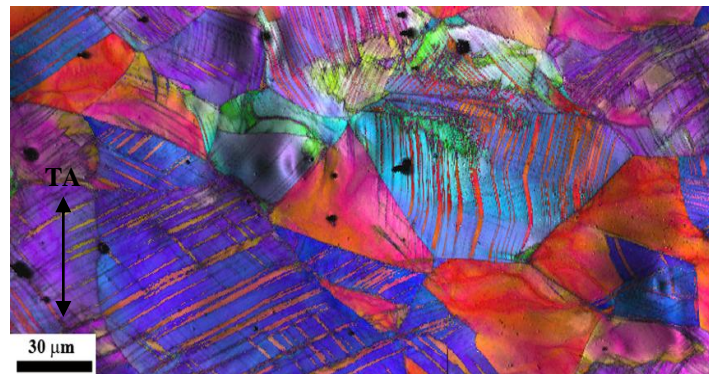


twins

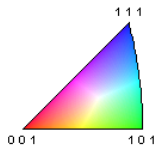
40%



20%



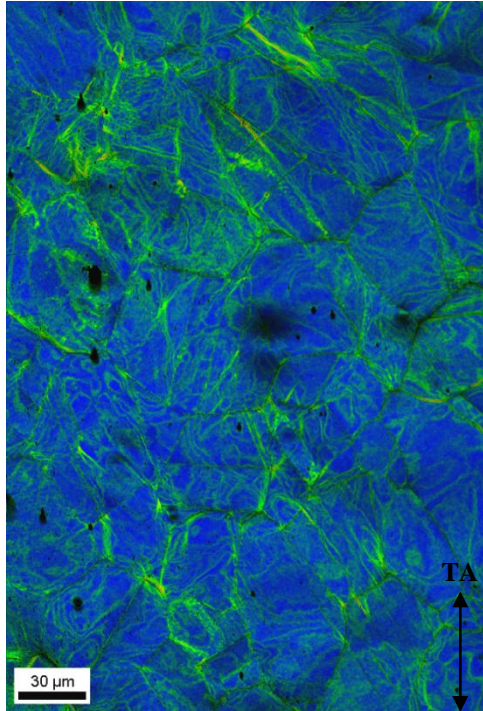
(High resolution
EBSD maps
Step size: 50-
100 nm)



Fe-22Mn-0.6C (wt%) TWIP steel

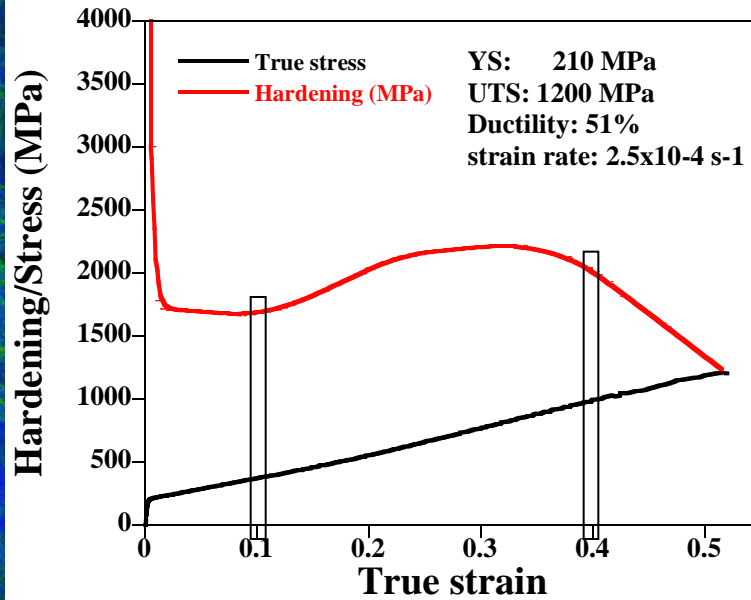
Tensile test at room temperature

10%



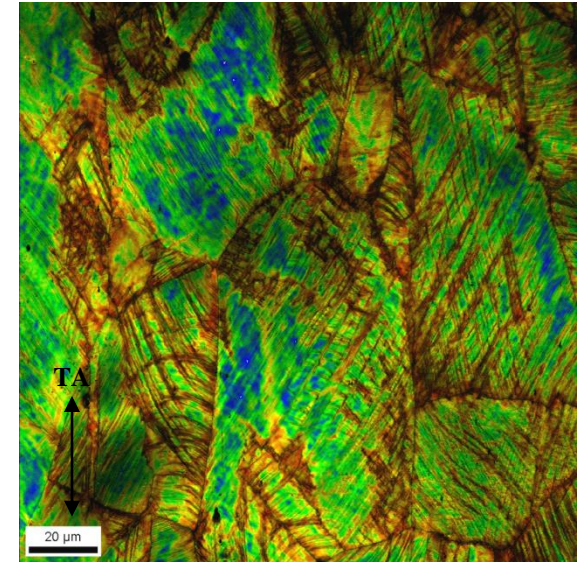
Color Coded Map Type: Local Orientation Spread

Min	Max	Total Fraction	Partition Fraction
0.213279	3.70073	0.997	0.997



20%

40%



Color Coded Map Type: Local Orientation Spread

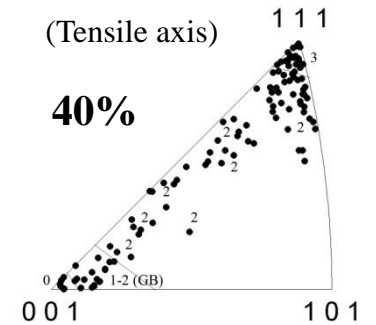
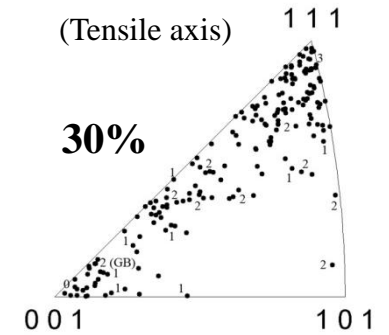
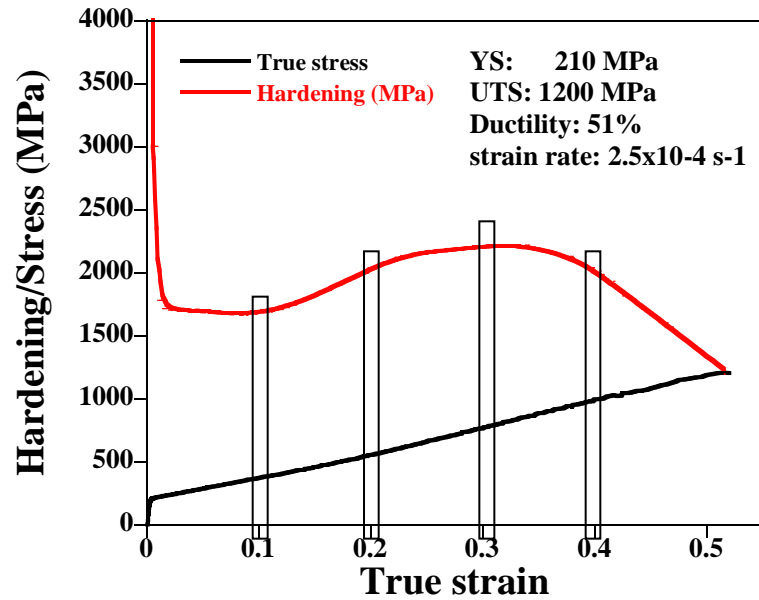
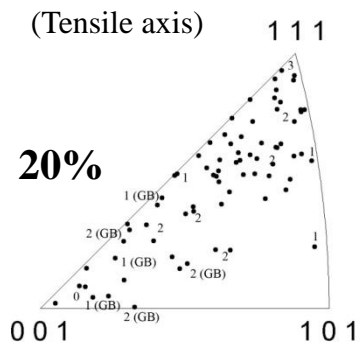
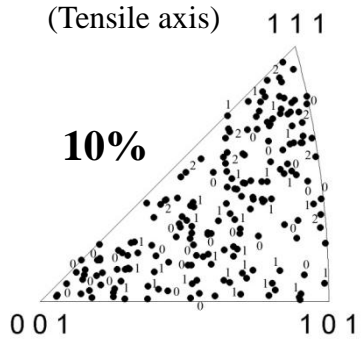
Min	Max	Total Fraction	Partition Fraction
0.5	3.5	0.995	0.995

Local Orientation
Spread Maps

Fe-22Mn-0.6C (wt%) TWIP steel

Tensile test at room temperature

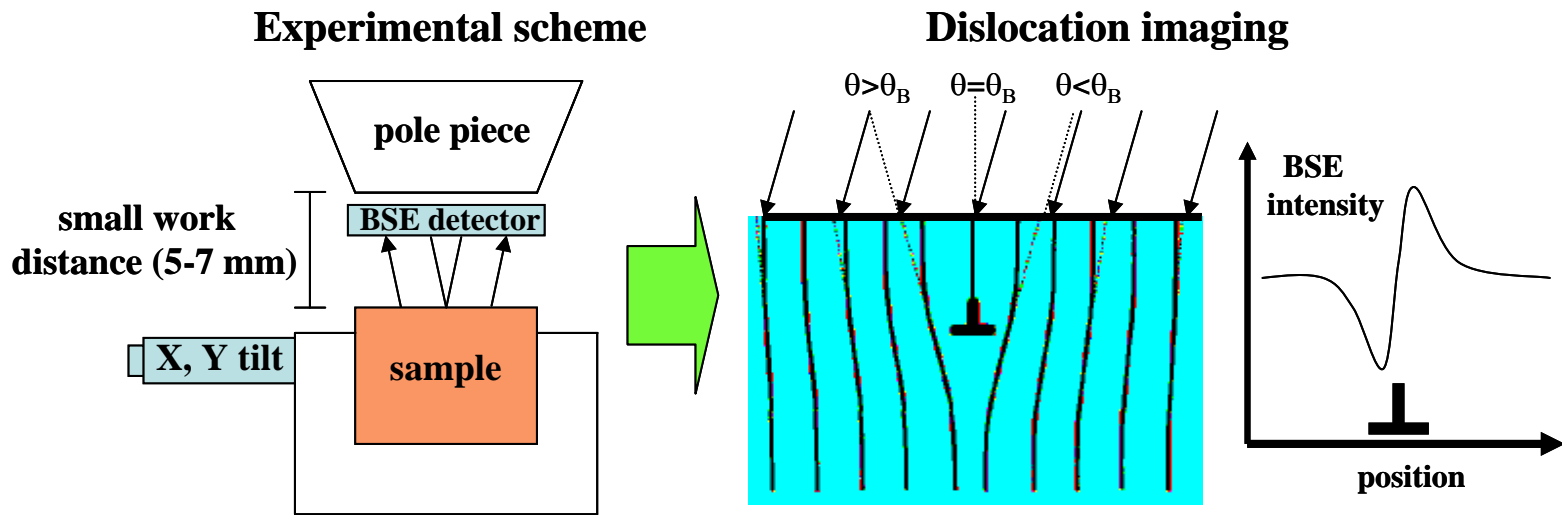
Inverse pole figures



- The spatial resolution of EBSD does not allow indexing of thin twins in TWIP steels (thickness: 30 nm).
- No information about defects is provided by EBSD

A new implementation of the technique ECCEI is being developed in SEM: QECCI

Quantitative Electron Channeling Contrast Imaging (QECCI)



It allows the observation of crystal defects like dislocations using SEM

Fe-22Mn-0.6C (wt%) TWIP steel

Comparison EBSD-QECCI

High resolution EBSD

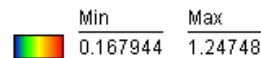
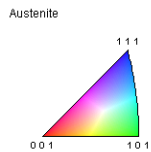
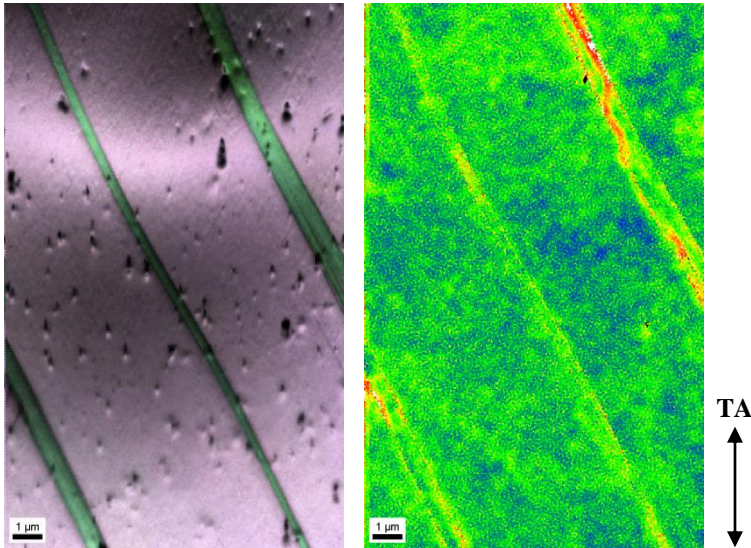
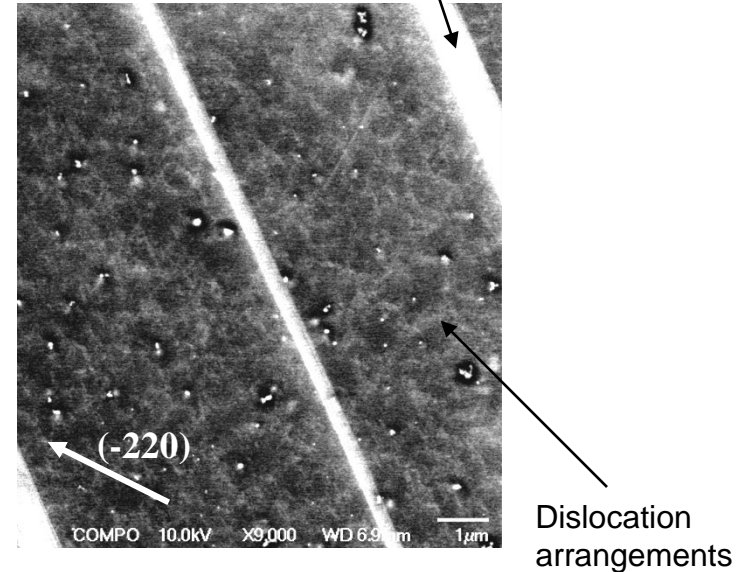


Image Quality Kernel Average Misorientation

blur contrast

QECCI



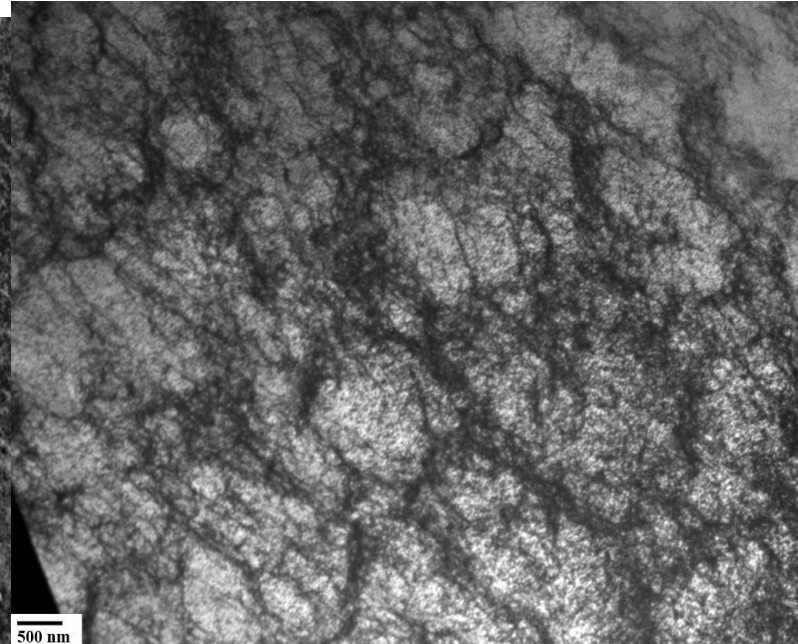
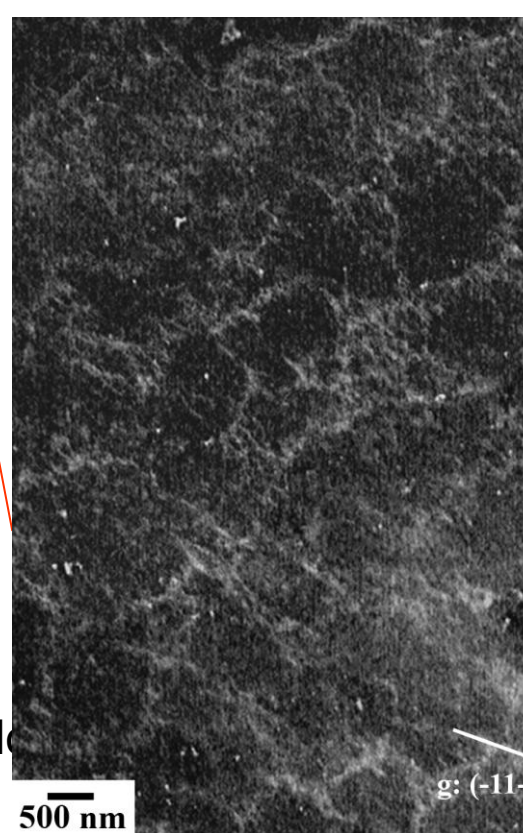
-QECCI provides detailed information on dislocation arrangements and dislocation-twin boundary interaction.

-Quantitative analysis is carried out with EBSD.

Fe-22Mn-0.6C (wt%) TWIP steel

QECCI

TEM-Bright Field



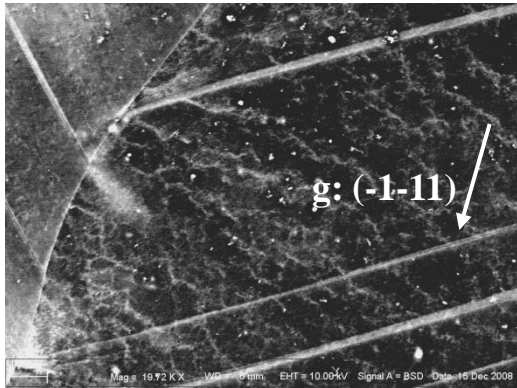
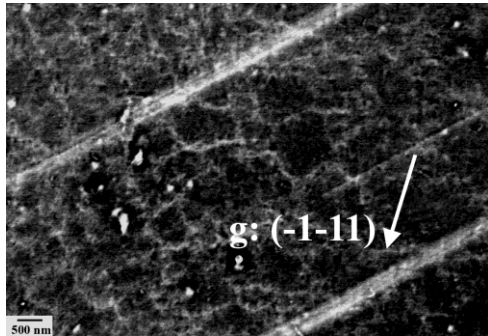
Dislo

g: (-11-1)

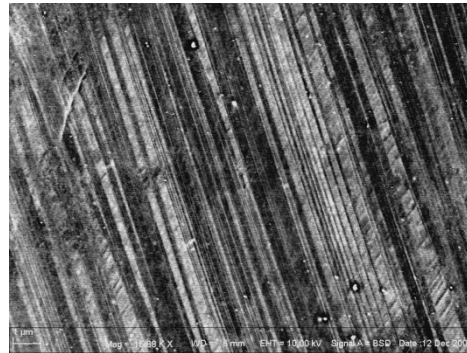
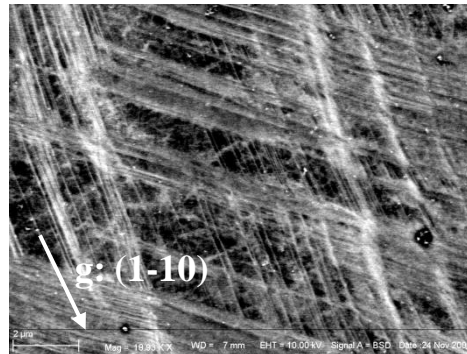
by QECCI

Fe-22Mn-0.6C (wt%) TWIP steel: examples of QECCI

10%



40%



Dislocation density measurement by electron channeling contrast imaging in a scanning electron microscope

I. Gutierrez-Urrutia* and D. Raabe

Max-Planck-Institut für Eisenforschung, Max-Planck Str. 1, D-40237 Düsseldorf, Germany

Received 12 October 2011; revised 18 November 2011; accepted 19 November 2011
Available online 30 November 2011

We have measured the average dislocation density by electron channeling contrast imaging (ECCI) in a scanning electron microscope under controlled diffraction conditions in a Fe–3 wt.% Si alloy tensile deformed to a macroscopic stress of 500 MPa. Under optimal diffraction conditions, ECCI provides an average dislocation density close to that obtained by bright-field transmission electron microscopy. This result confirms that ECCI is a powerful technique for determining dislocation densities in deformed bulk metals.

© 2011 Acta Materialia Inc. Published by Elsevier Ltd. All rights reserved.

Keywords: Dislocations; Low-temperature deformation; Electron diffraction; Scanning electron microscopy (SEM); Ferritic steels

The storage of dislocations during deformation of metals plays a key role in most metallurgical phenomena such as strain hardening, damage, creep, fatigue, athermal phase transformations, recrystallization and strain-induced grain boundary migration. In the former cases, it determines the mechanical properties such as strength and ductility. In the latter cases, it plays an important role in the mechanisms acting during annealing and transformation of deformed microstructures. In many cases, the average dislocation density is even linearly related to characteristic phenomena such as strengthening, creep rate, recovery and primary recrystallization. For this reason, the determination of the average dislocation density is important to better understand such phenomena. Dislocation density is commonly measured by direct methods such as transmission electron microscopy (TEM) [1–3] and indirect methods such as X-ray diffraction (XRD) [4,5]. TEM provides a highly accurate determination of the dislocation density provided that the dislocations can be clearly distinguished, i.e. it can be applied with high accuracy below a certain dislocation density ($\sim 5\text{--}10 \times 10^{-14} \text{ m}^{-2}$). However, the determination of average dislocation density values in heterogeneous microstructures by TEM is time consuming owing to the demanding sample preparation technique involved. On the other hand, XRD provides an average

dislocation density of the bulk deformed material in a shorter time but with a limited spatial resolution. In addition, XRD analysis of defect structures requires the use of a well-justified underlying model that connects a certain dislocation density and distribution with a total displacement gradient field.

An alternative microscopy technique for characterizing deformed microstructures is electron channeling contrast imaging (ECCI) [6–9]. ECCI is a scanning electron microscopy (SEM) technique that makes use of the fact that the backscattered electron intensity is strongly dependent on the orientation of the crystal lattice planes with respect to the incident electron beam due to the electron channeling mechanism. Slight local distortions in the crystal lattice due to dislocations cause a modulation of the backscattered electron intensity, allowing the defect to be imaged. The ECCI technique has been used to image dislocation structures in metals deformed during fatigue loading [10] or in the vicinity of cracks [11], and even stacking faults [12]. In particular, we have recently characterized complex mixed dislocation and twin substructures, as well as their individual contributions to strain hardening, on a highly deformed Fe–22 wt.% Mn–0.6 wt.% C alloy [13,14] by ECCI. For this purpose we used a novel ECCI set-up [9] which makes use of combined electron backscatter diffraction (EBSD) to image dislocations at enhanced contrast. In this paper, we demonstrate that the ECCI technique allows the determination of the average dislocation density of a deformed metal. The aim of the work is to establish ECCI

* Corresponding author. Tel.: +49 2116792 407; e-mail: i.gutierrez@mpie.de

as a very powerful, versatile, fast and experimentally robust method for determining dislocation defects densities and arrangements that involves a relatively simple preparation process. For this reason we used ECCI to measure the average dislocation density in a Fe–3 wt.% Si alloy tensile deformed to a macroscopic stress of 500 MPa. Under optimal diffraction conditions, the ECCI technique provides an average dislocation density close to that obtained by bright-field TEM.

The material selected was a Fe–3 wt.% Si alloy sheet 260 μm thick supplied by ThyssenKrupp Electrical Steel GmbH. The material has a large grain size in the centimeter range and a strong Goss texture $\{110\}\langle 001\rangle$. This microstructure makes the sample suited for the measurement of the dislocation density. Tensile tests were performed at room temperature at a strain rate of $2 \times 10^{-3} \text{ s}^{-1}$ to a macroscopic stress of 500 MPa. The mechanical tests were carried out using test instrument of Kammrath & Weiss GmbH (44141 Dortmund, Germany) equipped with a digital image correlation (DIC) system (ARAMIS system, GOM-Gesellschaft für Optische Messtechnik mbH, 38106 Braunschweig, Germany) for measuring the local strain. Details of this set-up are described in Ref. [15]. The surface pattern required for DIC was obtained as explained in Ref. [13]. Dislocation densities were measured in areas with a local strain of 0.05 by means of ECCI. A new recently reported set-up for ECCI [9] was used in this study to obtain ECCI images under controlled diffraction conditions which produced an enhanced dislocation contrast. This ECCI set-up has been successfully used in the imaging of dislocation substructures in Fe-based alloys [13,14]. The set-up uses EBSD patterns for calculating the optimal orientation of the crystal inspected through a specific combination of tilts and rotations. These are determined from the corresponding calculated diffraction pattern using the algorithm developed in Ref. [16]. ECCI observations were carried out in a Zeiss Crossbeam instrument (XB 1540, Carl Zeiss SMT AG, Germany) consisting of a Gemini-type field emission gun (FEG) electron column and a focused ion beam (FIB) device (Orsay Physics). ECCI was performed at 10 kV acceleration voltage and a working distance of 6 mm, using a solid-state four-quadrant backscattered electron detector. ECCI images were obtained with the sample normal aligned parallel to the incident electron beam.

It is well known that optimum dislocation contrast in ECCI is obtained by orienting the crystal to the exact Bragg angle, i.e. $s = 0$ where s is the deviation vector, in a two-beam condition [8,17]. Dislocation contrast becomes weaker under diffraction conditions deviating from the optimal, i.e. when $s \neq 0$. However, the latter, although not optimal, can be useful in the determination of the average dislocation density, as we show below. In the present work, we have evaluated the influence of diffraction condition in the determination of the average dislocation density. Dislocation densities were determined from ECC images that were taken under two different diffraction conditions, namely two-beam conditions with one set of hkl planes at the Bragg angle, and, alternatively, three-beam cases with two sets of hkl planes in an out-of-Bragg condition. For the first diffraction condition, dislocations appear as sharp bright lines

over a dark background, whereas in the second diffraction condition, dislocations are visible as bright and dark sharp lines over a brighter background.

Figure 1 shows examples of ECC images of dislocation arrangements at the same area under different diffraction conditions with the corresponding calculated diffraction patterns. The ECC image of Figure 1a was obtained after orienting the crystal into Bragg condition using a high-intensity reflection of (110)-type. The calculated diffraction pattern is shown in Figure 1b. Under this diffraction condition, the crystal matrix appears dark and dislocations appear as sharp bright lines. The ECC image presented in Figure 1c was obtained after orienting the crystal out of the Bragg condition with $s < 0$. The calculated diffraction pattern is shown in Figure 1d. In this orientation, the crystal matrix appears brighter than in Bragg condition due to electron channeling mechanism [8]. In the first case, electrons are more effectively channeled into the lattice and the backscattering yield is low, leading to a dark appearance of the crystal. In the second case, the backscattering yield is enhanced and the crystal appears bright. In Figure 1c, we can identify dislocations appearing as white and black lines with uniform and sharp contrast. According to the dislocation contrast theory developed for TEM, the dislocation contrast exhibits an oscillatory black–white color with a periodicity of ξ_g , where ξ_g is the extinction distance [3]. Spencer et al. [17] showed that in ECCI, similar to TEM, the oscillatory behavior disappears for a dislocation that is located deeper than $2\xi_g$ from the sample surface, due to anomalous absorption phenomena related with inelastic scattering processes. According to the dislocation contrast profiles calculated by the authors [11], in a two-beam condition with one set of hkl planes at or close to Bragg orientation, dislocations exhibit a uniform white contrast. As in ECCI the $g \cdot b = 0$ invisibility criterion holds [8,18,19], we can ascribe the bright sharp dislocations to those fulfilling $g \cdot b \neq 0$ with g : 110, where b is the Burgers vector and g the diffraction vector. The origin of the

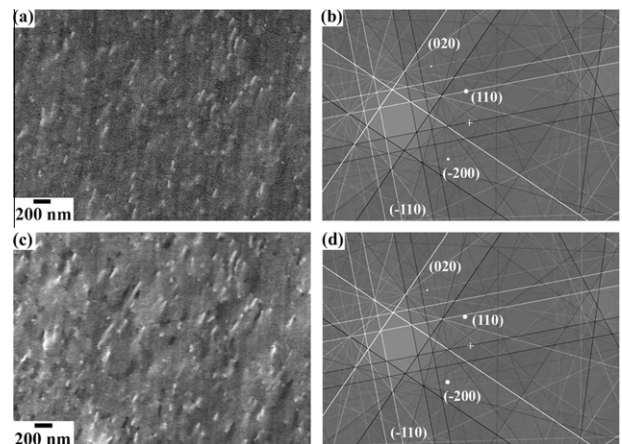


Figure 1. ECC images of dislocation arrangements of the same area in a Fe–3 wt.% Si alloy tensile deformed to a macroscopic stress of 500 MPa under two different diffraction conditions with the corresponding calculated diffraction pattern: (a and b) two-beam condition with g : 110 at Bragg orientation; (c and d) three-beam condition with g : 110 and g : –200 out-of-Bragg (g is the diffraction vector).

sharp black dislocation contrast observed in Figure 1c can be attributed to the deviation from the two-beam condition. As the calculated diffraction pattern of Figure 1d reveals, the (-200) reflector, which is out of Bragg condition with $s \ll 0$, is excited as well, although it is less strong than $g: 110$, i.e. it corresponds to a three-beam condition. Accordingly, these dislocations fulfill $g \cdot b \neq 0$ with $g: -200$ and, due to $s \ll 0$, exhibit a black contrast. In fact, this is the origin of the diffuse black dislocation contrast in the ECC image revealed in Figure 1a, as the calculated diffraction pattern of Figure 1b shows. Under the present microscope conditions with an acceleration voltage of 10 kV, anomalous absorption occurs at depths higher than about $2\xi_{200} \approx 26$ nm for the diffraction conditions used here. As most of the visible dislocations exhibit a uniform contrast, this indicates that dislocations visible by ECCI in the present study are placed deeper than 26 nm from the sample surface.

Average dislocation densities, ρ , were estimated using the relationship: $\rho = 2N/Lt$, where N is the number of dislocation lines intersecting a grid of total line length L on the corresponding ECC image and t is the probe depth. This is a standard relationship used in TEM when the individual dislocations can be clearly distinguished, like in the present study [1,20]. Dislocations were measured from ECC images similar to those shown in Figure 1. As example, Figure 2 depicts a drawing of the dislocations (black lines) imaged under the diffraction conditions of Figure 1a and c. Dislocations are identified according to the dislocation contrast of the corresponding diffraction condition, namely bright lines in Figure 1a and bright and dark lines in Figure 1c. Only dislocations with a well-defined and sharp contrast are considered. Figure 1c reveals that some dislocations with black contrast exhibit a blurred contrast, which is mainly ascribed to the multi-beam diffraction condition with $s < 0$. However, these dislocations can also be clearly identified. It can be seen

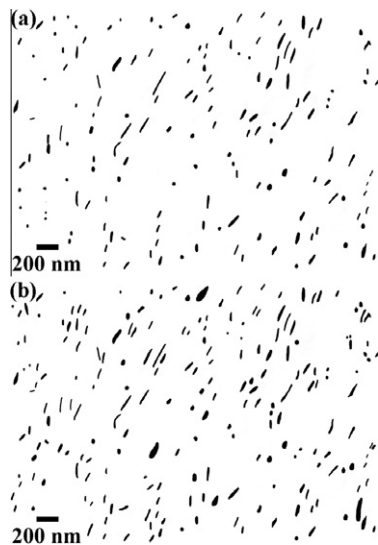


Figure 2. Schematic drawings of the dislocations (black lines) imaged by ECCI as shown in Figure 1: (a) corresponds to Figure 1a, (b) corresponds to Figure 1c. See the text for details of the identification procedure.

that the number of dislocations identified in Figure 2b is higher than in Figure 2a. This is ascribed to the higher number of excited reflectors which provides two types of dislocation contrast, i.e. black and white. The probe depth for imaging dislocations in ECCI is a difficult parameter to calculate due to the complexity of modeling the backscattering of electrons from a thick crystalline material. However, Wilkinson et al. [7] have calculated ECC image profiles of dislocations based on the theoretical approach of channeling contrast formation suggested by Spencer et al. [17], and estimated the limiting probe depth for imaging dislocations in ECCI, which is about $5\xi_g$. Assuming this probe depth and under the present ECCI conditions (acceleration voltage of 10 kV, and corresponding values of ξ_g for Fe [21]), the probe depth ranges from 45 to 65 nm for the diffraction vectors g used in the present study ((110) and (200) -type). The estimated average dislocation densities are plotted in Figure 3. Under three-beam conditions, the largest probe depth was used. Average dislocation densities of $10 \pm 4 \times 10^{-13}$ and $17 \pm 6 \times 10^{-13} \text{ m}^{-2}$ were obtained from the ECC images under two-beam conditions with one set of hkl planes at Bragg orientation and three-beam conditions with two sets of hkl planes out-of-Bragg, respectively. We should emphasize here that the multi-beam conditions used to estimate the average dislocation density are similar to those shown in Figure 1c and d. As Figure 1 reveals, the higher average density obtained by the second diffraction condition is ascribed to the higher number of excited reflectors, which provides, due to channeling mechanism, a higher amount of visible dislocations.

To compare the present estimations of the average dislocation density measured by ECCI to that determined by a standard characterization technique such as TEM, we have included in Figure 3 the average dislocation density measured in a Fe–3 wt.% Si sample deformed to the same macroscopic stress level (500 MPa) by bright-field TEM. The average dislocation density was measured from TEM micrographs using the same method as in the present work [22]. It can be seen that the average dislocation density estimated from ECCI is in the same range than that determined from bright-field

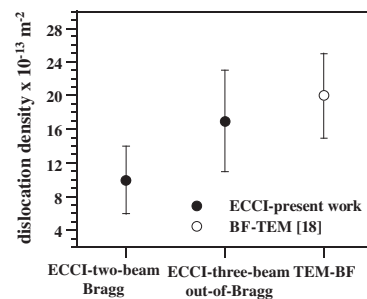


Figure 3. Average dislocation densities determined in a Fe–3 wt.% Si alloy tensile deformed to a macroscopic stress of 500 MPa by two different electron microscopy techniques: ECCI and TEM. Average dislocation densities were measured by ECCI under two different diffraction conditions: two-beam conditions with one set of hkl planes in the Bragg orientation (Fig. 1a and b) and three-beam diffraction conditions with two sets of hkl planes out-of-Bragg (Fig. 1c and d) (BF: bright field).

TEM. In particular, the average dislocation density measured by ECCI in two-beam conditions with one set of hkl planes at the Bragg orientation represents a lower-bound value for the dislocation density. This result is well-known from corresponding TEM-based estimates [1]. The present work shows that three-beam diffraction conditions with two sets of hkl planes out-of-Bragg provide a better estimation of the average dislocation density by ECCI, close to that obtained by bright-field TEM. Further, this study confirms ECCI as a powerful technique to determine dislocation densities in deformed bulk metals at a wide field of view. This is a significant advance in microstructural characterization of deformed materials where dislocation densities are typically determined by TEM or XRD. As ECCI is a SEM-based technique it has the advantage over TEM that much larger areas can be observed and samples are easier to prepare. However, due to the small size of the features imaged in this study, namely dislocation lines, the determination of dislocation densities is here performed on areas comparable to those used in TEM. Furthermore, in TEM, the wedge-shape geometry of the foil also makes it necessary to measure the sample thickness in each analyzed material portion. In ECCI, the probe depth only depends on the acceleration voltage and diffraction vector through the extinction distance. In particular, in an oxide-free surface and operating at constant acceleration voltage, the probe depth is only determined by the diffraction vector. It is worth mentioning that in the present ECCI–EBSD approach dislocations are imaged in the scanning electron microscope directly from the collected electron backscattered signal. Accordingly, the estimated dislocation density comprises both types of dislocations, namely geometrically necessary dislocations (GND) and statistically stored dislocations (SSD). Recently, there is an increasing interest in the determination of the GND density via EBSD-based approaches. These methods are based on the measurement of orientation gradients by electron backscatter diffraction patterns and the subsequent dislocation density tensor calculation [23–25]. Considering the current experimental limitations in the determination of orientation gradients via EBSD [26], these methods can provide microstructurally based insights into the mechanisms of strain hardening and size-dependent plasticity. However, the calculated dislocation density is a lower bound of the total dislocation density because only GNDs are considered. In this regard, the present ECCI–EBSD approach provides a better estimate of the total dislocation density, which is similar to that obtained by conventional TEM, as confirmed by the present results.

In summary, the average dislocation density in a Fe–3 wt.% Si alloy tensile deformed to a macroscopic stress of 500 MPa has been determined by ECCI using a novel SEM-EBSD-based set-up. We have studied the influence of the diffraction conditions on the measure-

ment of the dislocation density in ECCI. Under optimum diffraction conditions, ECCI provides an average dislocation density close to that obtained by standard bright-field TEM. This result confirms that ECCI is a powerful and versatile wide-field-of-view technique to determine dislocation densities in deformed metals.

The authors would like to acknowledge the financial support by the German Research Foundation in the framework of the SFB 761 “steel ab initio”.

- [1] P. Hirsch, A. Howie, R.B. Nicholson, D.W. Pashley, M.J. Whelan, *Electron Microscopy of Thin Crystals*, Robert E. Krieger, Huntington, NY, 1977.
- [2] G. Thomas, M.J. Goringe, *Transmission Electron Microscopy of Materials*, John Wiley & Sons, New York, 1979.
- [3] D.B. Williams, C.B. Carter, *Transmission Electron Microscopy. A Textbook for Materials Science*, Springer Verlag, Berlin, 2009.
- [4] T. Ungár, H. Mughrabi, M. Wilkens, *Acta Metall.* 30 (1982) 1861.
- [5] T. Ungár, S. Ott, P.G. Sanders, A. Borbély, J.R. Weertman, *Acta Mater.* 46 (1998) 3693.
- [6] D.C. Joy, D.E. Newbury, D.L. Davidson, *Rev. Phys. Appl.* 53 (1982) 81.
- [7] A.J. Wilkinson, G.R. Anstis, J.T. Czernuszka, N.J. Long, P.B. Hirsch, *Philos. Mag. A* 68 (1993) 59.
- [8] A.J. Wilkinson, P.B. Hirsch, *Micron* 28 (1997) 279.
- [9] I. Gutierrez-Urrutia, S. Zaefferer, D. Raabe, *Scr. Mater.* 61 (2009) 737.
- [10] Z.F. Zhang, Z.G. Wang, Z.M. Sun, *Acta Mater.* 49 (2001) 2875.
- [11] B.C. Ng, B.A. Simkin, M.A. Crimp, *Ultramicroscopy* 75 (1998) 137.
- [12] A. Weidner, S. Martin, V. Klemm, U. Martin, H. Biermann, *Scr. Mater.* 64 (2011) 513.
- [13] I. Gutierrez-Urrutia, S. Zaefferer, D. Raabe, *Mater. Sci. Eng. A* 527 (2010) 3552.
- [14] I. Gutierrez-Urrutia, D. Raabe, *Acta Mater.* 59 (2011) 6449.
- [15] D. Raabe, M. Sachtleber, Z. Zhao, F. Roters, S. Zaefferer, *Acta Mater.* 49 (2001) 3433.
- [16] S. Zaefferer, *J. Appl. Crystallogr.* 33 (2000) 10.
- [17] J.P. Spencer, C.J. Humphreys, P.B. Hirsch, *Philos. Mag.* 26 (1972) 193.
- [18] A.J. Wilkinson, P.B. Hirsch, *Philos. Mag. A* 72 (1995) 81.
- [19] M.A. Crimp, B.A. Simkin, B.C. Ng, *Philos. Mag. Lett.* 81 (2001) 833.
- [20] R.K. Ham, *Philos. Mag.* 69 (1961) 1183.
- [21] L. Reimer, H. Kohl, *Transmission Electron Microscopy. Physics of Image Formation*, Springer Verlag, Berlin, 2008.
- [22] D. Griffiths, J.N. Riley, *Acta Metall.* 14 (1966) 755.
- [23] E. Demir, D. Raabe, N. Zaafarani, S. Zaefferer, *Acta Mater.* 57 (2009) 559.
- [24] S. Sun, B.L. Adams, W.E. King, *Philos. Mag. A* 80 (2000) 9.
- [25] L.P. Kubin, A. Mortensen, *Scr. Mater.* 48 (2003) 119.
- [26] T.B. Britton, C. Maurice, R. Fortunier, J.H. Driver, A.P. Day, G. Meaden, D.J. Dingley, K. Mingard, A.J. Wilkinson, *Ultramicroscopy* 110 (2010) 1443.



The effect of grain size and grain orientation on deformation twinning in a Fe–22 wt.% Mn–0.6 wt.% C TWIP steel

I. Gutierrez-Urrutia*, S. Zaefferer, D. Raabe

Max-Planck-Institut für Eisenforschung, Max-Planck Str. 1, D-40237 Düsseldorf, Germany

ARTICLE INFO

Article history:

Received 14 December 2009

Received in revised form 10 February 2010

Accepted 11 February 2010

Keywords:

EBSD

Mechanical characterization

Steel

Twinning

ABSTRACT

We investigate the effect of grain size and grain orientation on deformation twinning in a Fe–22 wt.% Mn–0.6 wt.% C TWIP steel using microstructure observations by electron channeling contrast imaging (ECCI) and electron backscatter diffraction (EBSD). Samples with average grain sizes of 3 μm and 50 μm were deformed in tension at room temperature to different strains. The onset of twinning concurs in both materials with yielding which leads us to propose a Hall–Petch-type relation for the twinning stress using the same Hall–Petch constant for twinning as that for glide. The influence of grain orientation on the twinning stress is more complicated. At low strain, a strong influence of grain orientation on deformation twinning is observed which fully complies with Schmid's law under the assumption that slip and twinning have equal critical resolved shear stresses. Deformation twinning occurs in grains oriented close to $\langle 111 \rangle$ /tensile axis directions where the twinning stress is larger than the slip stress. At high strains (0.3 logarithmic strain), a strong deviation from Schmid's law is observed. Deformation twins are now also observed in grains unfavourably oriented for twinning according to Schmid's law. We explain this deviation in terms of local grain-scale stress variations. The local stress state controlling deformation twinning is modified by local stress concentrations at grain boundaries originating, for instance, from incoming bundles of deformation twins in neighboring grains.

© 2010 Elsevier B.V. All rights reserved.

1. Introduction

TWIP (twinning-induced plasticity) steels have received high interest in recent years due to their outstanding mechanical properties at room temperature combining high strength (ultimate tensile strength of up to 800 MPa) and ductility (elongation to failure up to 100%) based on a high work-hardening capacity [1–3]. TWIP steels are austenitic steels, i.e. face-centered cubic (fcc) metals, with high content in Mn (above 20% in weight %) and small additions of elements such C (<1 wt.%), Si (<3 wt.%), or Al (<3 wt.%). The steels have low stacking fault energy (between 20 and 40 mJ/m² [3–5]) at room temperature. Although the details of the mechanisms controlling strain-hardening in TWIP steels are still unclear, the high strain-hardening is commonly attributed to the reduction of the dislocation mean free path with the increasing fraction of deformation twins as these are considered to be strong obstacles to dislocation glide [3,6–8]. Therefore, a quantitative study of deformation twinning in TWIP steels is critical to understand their strain-hardening mechanisms and mechanical properties. Deformation twinning can be considered as a nucleation and growth process [9]. Twin growth is assumed to proceed by co-operative

movement of Shockley partials on subsequent $\{111\}$ planes. Possible mechanisms for the co-operative movement are the pole mechanism [10], a cross-slip mechanism [11] or the reaction between primary and secondary slip systems [12,13]. Nucleation of deformation twins, on the other hand, consists in the formation of the dislocation structures required for twin growth and a number of experimental observations suggest mechanisms for that [9,14,15]. Dislocation slip is therefore a prerequisite for twin formation. The stress required to produce twins in a microstructure, generally termed as twinning stress, is a mixture of the stress for twin nucleation and that for growth. However, as the experimental determination of the stress needed for twin nucleation is very difficult to accomplish [9], it is commonly assumed that the twin nuclei already exist and, hence, only the stress for twin growth can be experimentally measured which is generally identified as the twinning stress. As the growth of a deformation twin is controlled by the glide of Shockley partials, it is reasonable to assign a critical resolved shear stress on the slip plane to this process that must be reached to move the twinning dislocations leading to the deformation twinning. For the same material in an undeformed state, the main parameters that may influence the twinning stress and, hence, the twinning microstructure, are grain size and grain orientation. Only few studies have addressed the influence of these microstructural parameters on deformation twinning in TWIP steels [5,16,17]. Ueji et al. [5] reported a strong

* Corresponding author. Tel.: +49 2116792 211.

E-mail address: i.gutierrez@mpie.de (I. Gutierrez-Urrutia).

influence of grain size on deformation twinning in a Fe–31 wt.% Mn–3.0 wt.% Al–3.0 wt.% Si TWIP steel. They observed that deformation twinning is strongly inhibited for an average grain size of 1.8 μm suggesting that deformation twinning in TWIP steels becomes difficult as the grain size decreases to a certain scale. Yang et al. [16] and Meng et al. [17] reported a strong influence of grain orientation on twinning behavior in a Fe–33 wt.% Mn–3.0 wt.% Al–3.0 wt.% Si TWIP steel. They found that deformation twinning is favored during tension because the grains rotate towards the $\langle 111 \rangle$ /tensile axis which renders the crystals favorably oriented for twinning (high Schmid factor) whereas deformation twinning is suppressed during compression because the grains rotate towards the $\langle 101 \rangle$ axis which renders them unfavorably oriented for twinning (small Schmid factor). However, there are still some details that remain unclear regarding the influence of grain size and grain orientation on twinning behaviour in TWIP steels, in particular their role on the twinning stress. The aim of this report is to investigate in detail the influence of grain size and grain orientation on the twinning behavior in a Fe–22 wt.% Mn–0.6 wt.% C TWIP steel. Detailed microstructural observations by electron channeling contrast imaging (ECCI) and electron backscatter diffraction (EBSD) were performed on tensile deformed samples at room temperature to different strains with average grain sizes of 3 μm and 50 μm . Further analyses based on stress–strain curves and deformed microstructures were carried out to illustrate the effect of grain size and grain orientation on the twinning stress.

2. Experimental details

The TWIP steel used in this study had the chemical composition Fe–22 wt.% Mn–0.6 wt.% C. The material was melted in an induction furnace under Ar atmosphere and cast to round bars of 25 mm diameter. To avoid Mn segregation [18] samples were swaged to 20% area reduction at 1000 °C and subsequently solution-treated for 4 h at 1100 °C under Ar. Thereafter, samples were hot-rolled to 75% reduction in thickness at 1000 °C followed by air cooling. The hot-rolled material was then cold rolled to 70% thickness reduction. In order to obtain different grain sizes, the material was finally annealed at 700 °C for 5 or 15 min resulting in material with average grain size of 3 μm (referred to as steel FG) and 50 μm (referred to as steel LG), respectively. Tensile tests were carried out at room temperature at a strain rate of $5 \times 10^{-4} \text{ s}^{-1}$ to different strains. The tensile bone-shaped samples had 8 mm gage length, 2 mm gage width and 1 mm gage thickness. The monotonic tensile deformation experiments were carried out on a tensile test instrument Kammrath & Weiss GmbH (44141 Dortmund, Germany) equipped with a digital image correlation (DIC) system (ARAMIS system, GOM-Gesellschaft für Optische Messtechnik mbH, 38106 Braunschweig, Germany) to measure the local and macroscopic strain distribution. Details of this setup are described in [19–22]. The surface pattern required for DIC was obtained by applying two different colour sprays on the sample surface. Firstly, a white spray was used to obtain a homogeneous background and thereafter, a black spray was applied to obtain a spotted pattern. Averaged engineering strain values are obtained from the corresponding maps and utilized to calculate the logarithmic stress–strain values.

Deformation microstructures of the tensile deformed TWIP steels were examined by two scanning electron microscopy techniques: electron back scatter diffraction (EBSD) and electron channeling contrast (ECCI). The EBSD technique was used to analyze the local texture in relation with the microstructure. Orientation maps were performed in a 6500 F JEOL field emission gun-scanning electron microscope (FEG-SEM) equipped with a TSL

OIM EBSD system. EBSD maps were measured at 15 kV acceleration voltage and a working distance of 15 mm. The ECCI technique has been recently proven as a powerful technique to image deformation twins and even dislocation structures in TWIP steels by using a SEM [23]. A new recently reported setup for ECCI [23] was used in this study to obtain ECCI images under controlled diffraction conditions with enhanced dislocation and interface contrast. ECCI observations were carried out in a Zeiss Crossbeam instrument (XB 1540, Carl Zeiss SMT AG, Germany) consisting of a Gemini-type field emission gun (FEG) electron column and an focused ion beam (FIB) device (Orsay Physics). ECCI was performed at 10 kV acceleration voltage and a working distance of 6 mm, using a solid-state 4-quadrant BSE detector. The microscope was run in the “high current” mode and an objective lens aperture of 120 μm was used.

3. Results

3.1. Effect of grain size

The initial hot-rolled state of both materials (LG and FG) showed a fully austenitic structure which remained stable during deformation. No evidence of ϵ -martensite was detected by EBSD. The initial hot-rolled textures on both materials were weak, and during tensile deformation both steels developed similar deformation textures which are shown below. The similarity of deformation textures allows us to analyze the influence of grain size on deformation twinning by examining the deformation microstructures in samples LG and FG at similar strain levels.

The ECCI technique was found to be an excellent tool in examining deformation microstructures of TWIP steels. The onset of deformation twinning in steel LG was observed at a logarithmic strain of 0.03. At this strain level the twin fraction was very small (twin area fraction less than 0.001 determined from ECCI pictures of around 100 grains) and only few grains, less than 20%, contained deformation twins. In most of these grains only one twinning system (primary system) was activated. Fig. 1(a) shows an ECCI image of the microstructure of steel LG tensile deformed to 0.03 logarithmic strain. Grains containing deformation twins up to 50 μm in length and 0.5 μm in thickness, which are nucleated at grain boundaries, are visible. This ECCI image was obtained by orienting the grain in the centre of the image into Bragg condition for the diffraction vector $g: (1\bar{1}1)$. Under this diffraction condition, details of deformed microstructure such as deformation twins, orientation gradients (grey areas), and even dislocation structures can be identified at optimum contrast. At higher magnification it is further observed that deformation twins are not single but bundles consisting of thinner twins, as shown in Fig. 1(b). For this ECCI image optimum contrast was achieved by tilting the sample such as to excite the (002) diffraction vector of the twins in a “two-beams” condition. It is observed that the bundle, around 0.5 μm thick, consists of six thin twins (dark straight lines) with thickness values ranging from 30 nm to 200 nm. Increasing the strain to a logarithmic strain of 0.3 lead to a significant increase in the twin area fraction from zero to around 0.2, Fig. 1(c). Almost all the grains contained deformation twins activated in several systems (up to three activated twinning systems were observed in the same grain) and only less than 10% of the grains contained no twins. The microstructure was very heterogeneous consisting of grains with only the primary twinning system activated, grains with more than one twinning system activated (primary and secondary twinning systems), and grains with no twins.

Deformation twins were also observed by ECCI in steel FG deformed to low strains. Fig. 2(a) shows an ECCI image of the microstructure of steel FG deformed to 0.04 logarithmic strain.

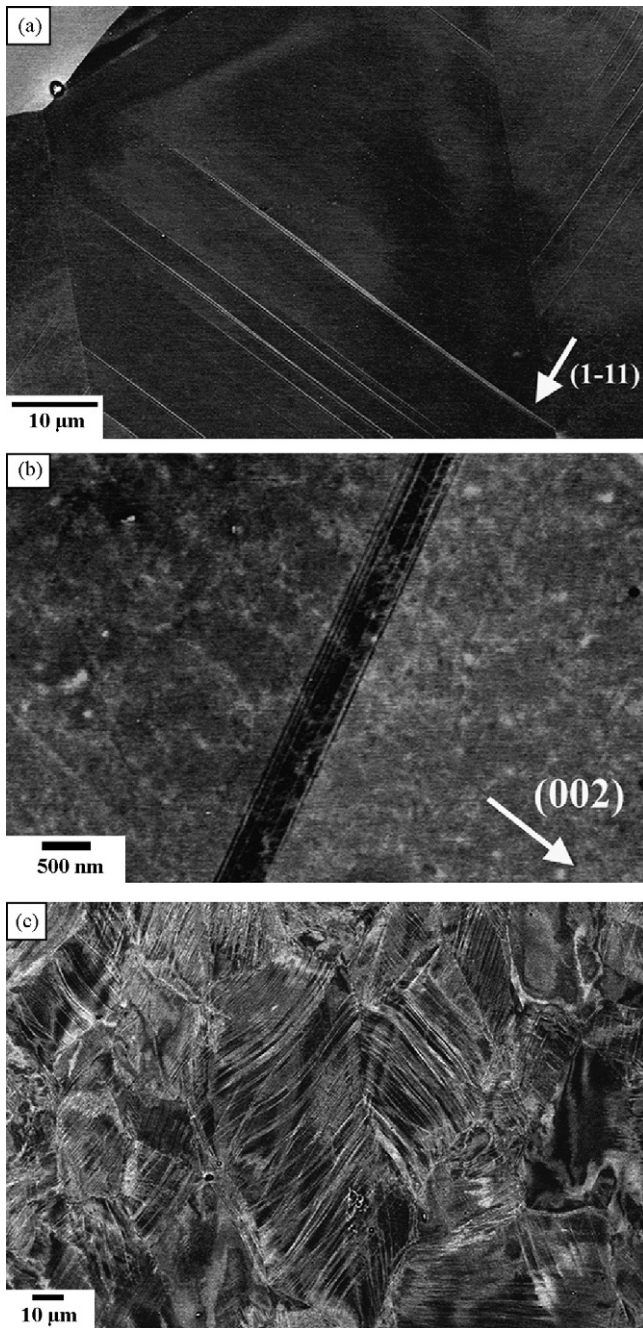


Fig. 1. Microstructures of steel LG (average grain size $50\ \mu\text{m}$) tensile deformed to 0.03 logarithmic strain (a and b) and 0.3 logarithmic strain (c). (a) ECCI image obtained in a SEM of grains containing bundles of deformation twins: diffraction vector $g: (1\ \bar{1}\ 1)_{\text{matrix}}$; (b) ECCI image of detail of a bundle containing thin twins (dark lines): diffraction vector $g: (0\ 0\ 2)_{\text{twin}}$.

Grains containing thin deformation twins (thickness 50–100 nm) are clearly observed, some of these twins are indicated with black arrows. Deformation twins were found even in grains smaller than $1\ \mu\text{m}$. Nevertheless, at this strain level the twin area fraction was very small, almost zero. At a higher logarithmic strain of 0.3 there was a significant increase in the twin area fraction, from zero to around 0.1. This increase in the twin area fraction is, however, smaller than in steel LG for the same strain level. Fig. 2(b) shows an ECCI image of the microstructure of steel FG strained to 0.3 logarithmic strain. The microstructure is very heterogeneous, like that observed for steel LG, containing grains with twins and grains with no twins. Most of the grains contained twins (around 80%) with

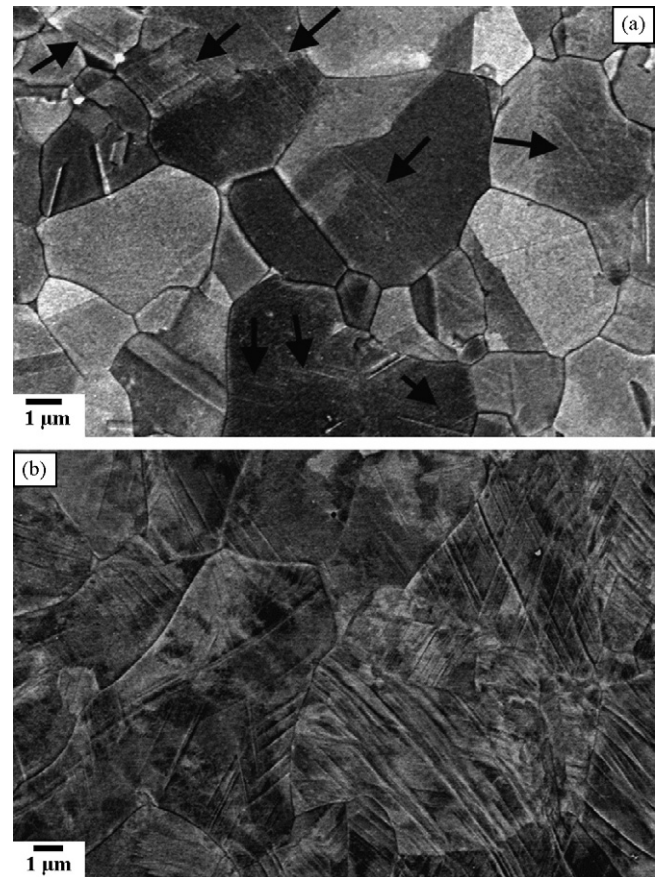


Fig. 2. ECCI images of microstructures containing deformation twins of steel FG (average grain size $3\ \mu\text{m}$), tensile deformed to 0.04 logarithmic strain (a) and 0.3 logarithmic strain (b). Black arrows indicate deformation twins.

different primary and secondary twinning systems activated.

3.2. Effect of grain orientation

We study the influence of grain orientation on deformation twinning during tensile deformation at room temperature on steel LG by means of EBSD. EBSD maps are displayed as image quality (IQ) maps and inverse pole figure (IPF) maps in the direction of tensile axis (TA). For better understanding of the influence of grain orientation on twinning, we analyze two deformation states: one at low strain (0.05 logarithmic strain) and another one at large strain (0.3 logarithmic strain).

Fig. 3(a) shows the inverse pole figure for the crystal direction along the tensile axis (TA-IPF) of the initial hot-rolled state indicating a weak texture of the starting state. Figs. 3(b) and (c) show TA-IPFs of the steel deformed to low and high strains, respectively. We observe that texture sharpens during tensile deformation, leading to texture components characterized by $\langle 111 \rangle // \text{TA}$ and $\langle 001 \rangle // \text{TA}$. Similar textures have been observed before in tensile deformed TWIP steels at room temperature [5,24]. Fig. 4 presents an example of an EBSD map performed on a sample strained to 0.05 logarithmic strain. As some twins are thinner than the resolution limit of the EBSD map, the TA-IPF map of Fig. 4(b) reveals a reduced number of indexed twins. However, in the image quality (IQ) map of Fig. 4(a) a higher number of twins is visible, appearing as straight thin dark lines. At this strain level, around one-third of the grains contained twins, mainly with only the primary twinning system activated. Fig. 5 shows a typical EBSD map performed on a sample strained to 0.3 logarithmic strain. At this strain level, bundles of twins were normally thicker than 100 nm and, therefore, most of

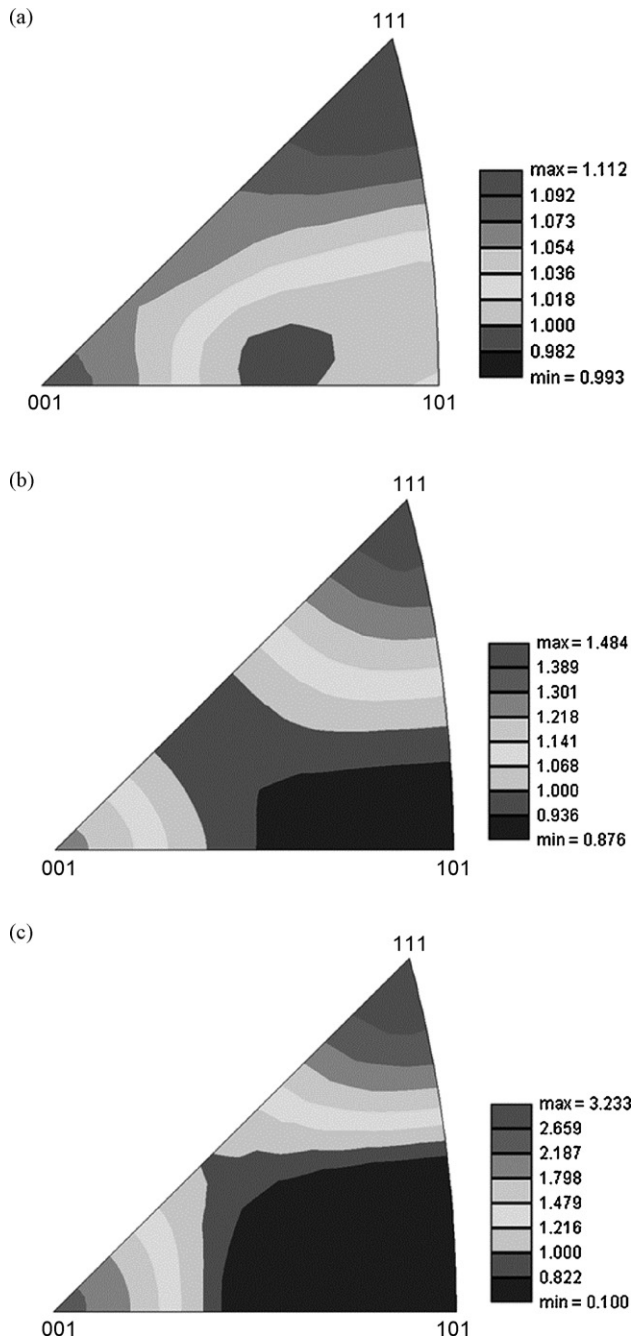


Fig. 3. Inverse pole figures along tensile axis direction of steel LG (average grain size $50\ \mu\text{m}$) at different states: as hot-rolled (a); tensile deformed to 0.03 logarithmic strain (b); tensile deformed to 0.3 logarithmic strain (c).

the twins can be indexed in the TA-IPF map. This figure shows that most of the grains, around 90%, contained deformation twins with several secondary activated twinning systems.

In order to study the influence of grain orientation on deformation twinning around 100 grains were analyzed in each deformation state. The orientation dependence of deformation twinning of steel LG to low strain and high strains is shown in Fig. 6(a) and (b), respectively. These TA-IPFs show orientations of grains containing twins (black dots) and of grains without twins (red dots). The TA-IPF of Fig. 6(a) shows that in the weakly strained LG sample there is a strong influence of the grain orientation on twinning activity. Deformation twinning mainly occurs in grains that are oriented close to the $\langle 111 \rangle // \text{TA}$ directions and only a small

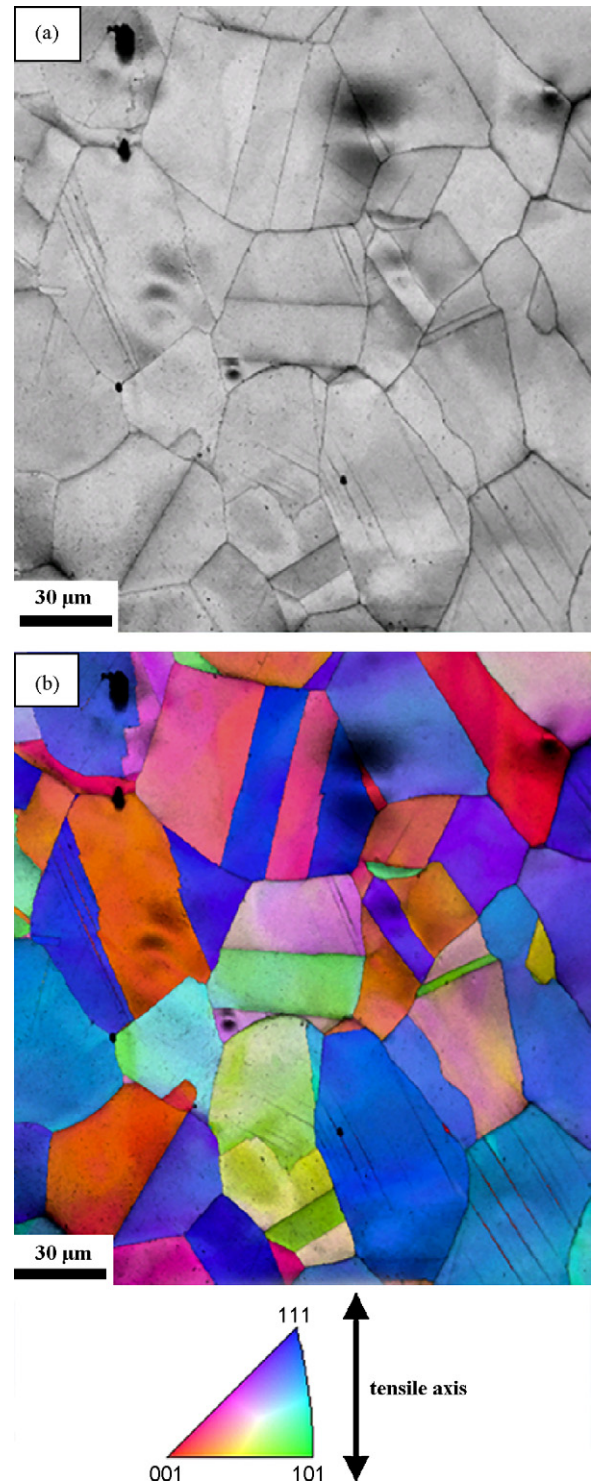


Fig. 4. EBSD map of steel LG (average grain size $50\ \mu\text{m}$) tensile deformed to 0.05 logarithmic strain. Diffraction pattern quality map (a), TA-IPF map (b) (TA: tensile axis; IPF: inverse pole figure).

fraction of grains with other orientations contain twins. Interestingly, at higher strain the influence of grain orientation on twinning activity decreased significantly. The TA-IPF given in Fig. 6(b) shows that in the highly strained LG sample, grains with almost all occurring orientations contained deformation twins and only grains oriented close to $\langle 001 \rangle // \text{TA}$ directions with angular deviation less than 5° contained no twins.

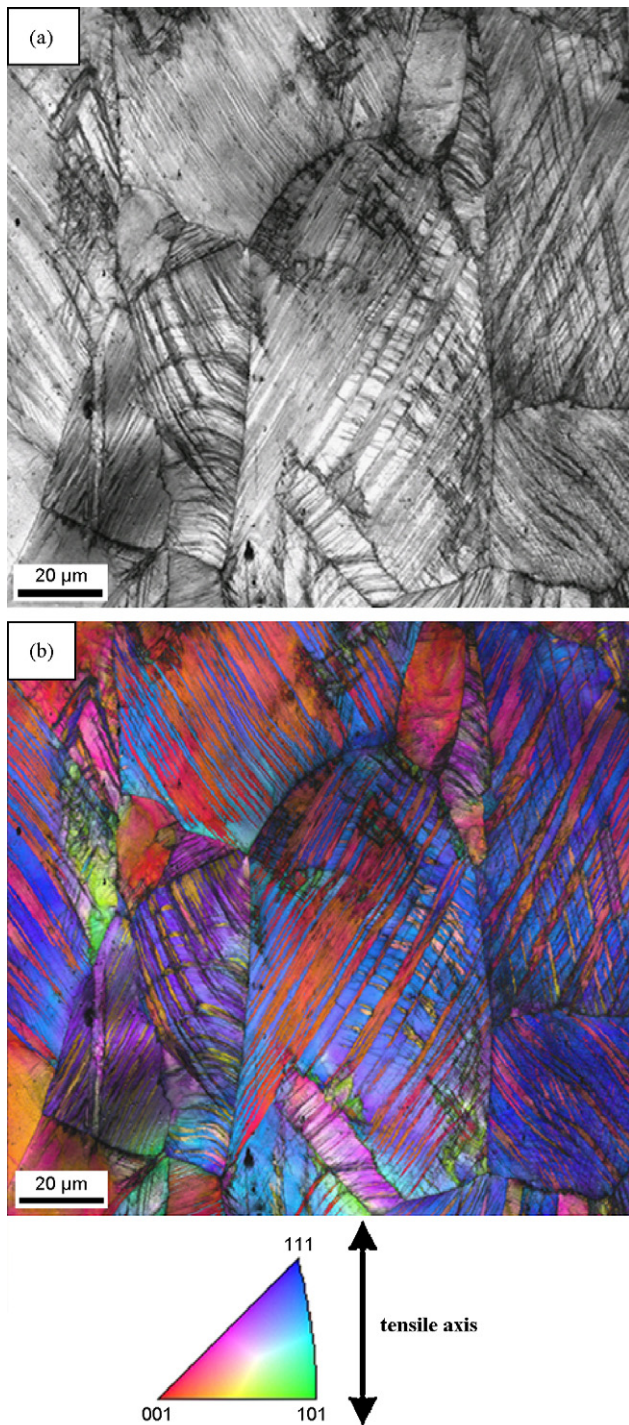


Fig. 5. EBSD map of steel LG (average grain size 50 μm) tensile deformed to 0.3 logarithmic strain. Diffraction pattern quality map (a), TA-IPF map (b) (TA: tensile axis; IPF: inverse pole figure).

4. Discussion

4.1. Effect of grain size

The main finding concerning the influence of grain size on deformation twinning is that grain refinement within the micrometer range does not suppress deformation twinning for the present TWIP steel tensile deformed at room temperature. Deformation twinning becomes more difficult as the average grain size decreases to 3 μm but it is not completely suppressed. Grain refinement pro-

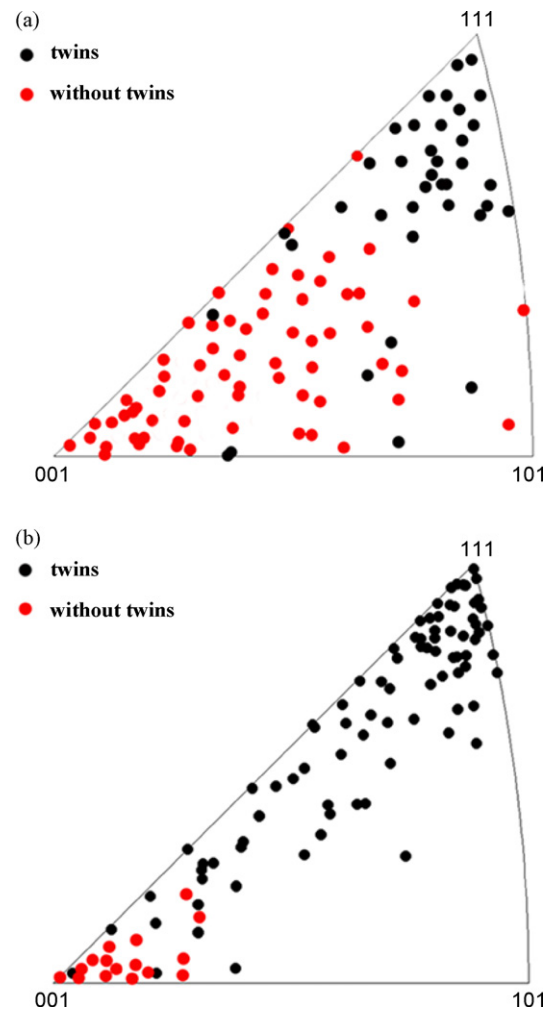


Fig. 6. Inverse pole figures along the tensile axis direction of steel LG (average grain size 50 μm) tensile strained to 0.05 logarithmic strain (a) and 0.3 logarithmic strain (b), respectively, showing grain orientations containing deformation twins (black dots) and without deformation twins (red dots). (For interpretation of the references to color in this figure legend, the reader is referred to the web version of the article.)

duces a strong decrease in the twin area fraction, from 0.2 for an average grain size of 50 μm to 0.1 for an average grain size of 3 μm at 0.3 logarithmic strain, but deformation twinning is still regularly observed in fine grains. As deformation twins are responsible for the outstanding mechanical properties of TWIP steels, this indicates that it is feasible to tailor the mechanical properties of Fe–22 wt.% Mn–0.6 wt.% C TWIP steels with grain refinement within the micrometer range. This is an interesting result regarding the optimization of the mechanical properties of TWIP steels. However, this result can at this stage not be generalized to other TWIP steel systems. For instance, Ueji et al. [5] reported a strong reduction in twinning activity in a Fe–31 wt.% Mn–3.0 wt.% Al–3.0 wt.% Si TWIP steel after similar grain refinement (average grain size of 1.8 μm) using also similar deformation conditions. The only difference is that the stacking fault energy (SFE) in Fe–31 wt.% Mn–3.0 wt.% Al–3.0 wt.% Si TWIP steel is larger than in the present Fe–22 wt.% Mn–0.6 wt.% C TWIP steel (around 40 mJ/m^2 against 22 mJ/m^2 [4,15]). These results indicate that the stacking fault energy, determined by chemical composition, plays a key role for the twinning behaviour in TWIP steels. Therefore, for a better understanding of twinning in TWIP steels both parameters, i.e. stacking fault energy and grain size, must be considered.

The influence of SFE on twinning is commonly considered as follows: Dislocation based models for deformation twinning in fcc

metals [10–13] propose that twinning is controlled by the glide of Shockley partials with Burgers vector $1/6 \langle 112 \rangle$ on $\{111\}$ planes. The critical resolved shear stress, τ_{critical} , to separate the leading Shockley partial from its trailing counterpart and thus create a twin is determined by a balance between the repulsive forces among the two Shockley partials and the attractive force of the SFE, given by

$$\tau_{\text{critical}} = \frac{\gamma}{b} \quad (1)$$

where γ is the SFE and b is the Burgers vector. As mentioned before, these models assume that twin nuclei already exist and therefore, only the stress for twin growth is estimated. Further, these models neither take into account the sources of dislocations nor a possible pile-up of dislocations in or at boundaries, thus the proposed twinning stress, τ_{critical} , can be considered as the twinning stress for a single crystal. The effect of grain size on deformation twinning still remains unclear. However, two approaches have been proposed to include the effect of grain size on twinning stress. In one approach [25] a Hall–Petch-type relation is proposed:

$$\tau_{\text{tw}} = \tau_0 + \frac{K_{\text{tw}}^{\text{H-P}}}{\sqrt{D}} \quad (2)$$

where τ_0 is the twinning stress for a single crystal, i.e. $\tau_0 = \tau_{\text{tw}} (D = \infty)$, and $K_{\text{tw}}^{\text{H-P}}$ is the Hall–Petch constant for twinning and D is the grain size. As explained above τ_0 can be replaced by γ/b leading to

$$\tau_{\text{tw}} = \frac{\gamma}{b} + \frac{K_{\text{tw}}^{\text{H-P}}}{\sqrt{D}} \quad (3)$$

This is a phenomenological relation which applies in many metals with different crystallographic structures such as hexagonal, bcc and fcc. Further, it has been reported that the Hall–Petch constant for twinning $K_{\text{tw}}^{\text{H-P}}$ is higher than that for slip $K_{\text{slip}}^{\text{H-P}}$ (for instance 10 times higher in Zr [26] and 2 times in copper [27]), although the reason for this difference is not well understood [25]. The other approach [28] proposes that the shear stress required to activate a twinning dislocation source is given by the shear stress to activate a Frank–Read source, $\tau_{\text{F-R}}$:

$$\tau_{\text{F-R}} = \frac{Gb}{2R} \quad (4)$$

where G is the shear modulus, b the Burgers vector and R the radius of the dislocation source. As twins are mainly nucleated at grain boundaries and the size of the softest possible dislocation source is proportional to the grain size, the following relation for the critical resolved shear stress for twinning is proposed:

$$\tau_{\text{tw}} = \frac{Gb}{D} \quad (5)$$

where G is the shear modulus, b is the Burgers vector and D is the grain size. This equation only describes the stress for nucleation of twins on boundaries. The growth of a twin in a homogeneous, single crystal matrix, however, is not considered. This growth stress is in principle the stress to drive the partial dislocations away from each other and may therefore be given by γ/b [10–13]. As a first approximation it should be independent of the grain size and can therefore be added to the nucleation stress, resulting in

$$\tau_{\text{tw}} = \frac{\gamma}{b} + \frac{Gb}{D} \quad (6)$$

In more detail, the grain size should have an effect, however, as grain size influences the yield stress which influences the hydrostatic pressure, which finally influences the stacking fault formation.

The examination of tensile strained samples by means of the ECCI technique reveals that deformation twinning occurs in both TWIP steels (steel LG and steel FG) at around 0.03 logarithmic strain.

This observation indicates that in the present TWIP steel deformation twinning initiates already at very low plastic strain, close to yielding. This result is consistent with previous observations by TEM in the same TWIP steel tensile deformed at room temperature where deformation twins were observed at 0.02 logarithmic strain [24]. Further studies on deformation twinning in fcc metals have also reported that deformation twinning is observed at small plastic strains [9,24,29]. However, the logarithmic stress at which deformation twinning was already activated (experimental twin stress) was higher in steel FG than in steel LG (steel FG: 400 MPa, steel LG: 270 MPa). This result indicates a clear effect of grain size on twin stress. However, this influence is not direct but indirect via slip, i.e. grain size mainly has an effect on slip. In fcc metals it has been observed that multiple slip is required for twinning, i.e. slip precedes twinning [9,12,29]. As explained above, in the present TWIP steel once multiple slip is activated deformation twinning occurs directly. These observations indicate a strong correlation between slip and twinning. As slip is influenced by the grain size via Hall–Petch a Hall–Petch-type dependence in twinning can therefore be expected. Table 1 shows the twinning stresses calculated from relations (3) and (6) for the present Fe–22 wt.% Mn–0.6 wt.% C TWIP steel. These stresses were calculated according to $\sigma_{\text{tw}} = \tau_{\text{tw}}/m$ assuming an average Schmid factor m of 0.326 [30], $\gamma = 22 \text{ mJ/m}^2$ [15], $b = 2.5 \times 10^{-10} \text{ m}$ [6], $G = 65 \text{ GPa}$ [6] and $K_{\text{tw}}^{\text{H-P}} = 356 \text{ MPa } \mu\text{m}^{1/2}$ [31]. As $K_{\text{tw}}^{\text{H-P}}$ is unknown $K_{\text{slip}}^{\text{H-P}}$ was used instead. Experimental twinning stresses are shown in the last column of Table 1. It can be seen that relation (3) overestimates the twinning stress but the grain size effect is properly reflected. Relation (6) estimates with high accuracy the twinning stress for an average grain size of $50 \mu\text{m}$ but provides a weak grain size dependence, which is not in agreement with experimental observations. These results suggest that in the micrometer range of the grain sizes studied in this work a Hall–Petch relation provides a good estimation of the influence of the grain size on the twinning stress.

It should be pointed out that the twinning stresses shown in Table 1 are calculated assuming $K_{\text{tw}}^{\text{H-P}} \sim K_{\text{slip}}^{\text{H-P}}$. Remarkably, this assumption provides reasonable twinning stresses suggesting that in the present TWIP steel $K_{\text{tw}}^{\text{H-P}} \leq K_{\text{slip}}^{\text{H-P}}$. This is a surprising result as there are very few studies reporting such behaviour [25]. Two significant conclusions can be obtained from this finding: (i) the effect of grain size on twinning stress is similar than on yield stress. Dislocation based models [10–13] propose that in fcc metals some specific dislocation reactions are needed to form a twin nucleus that subsequently evolves into a twin. It is also reported that in order to form such dislocation reactions multiple slip must be activated [9,12,29]. The experimental observation that deformation twinning occurs at small plastic strain close to yielding indicates that once multiple slip is activated deformation twinning occurs directly. $K_{\text{slip}}^{\text{H-P}}$ provides the resistance to slip propagation associated with the grain boundaries. The relation $K_{\text{tw}}^{\text{H-P}} \leq K_{\text{slip}}^{\text{H-P}}$ therefore indicates that the effect of grain size within the micrometer range on the twinning stress is mainly ascribed to the resistance to slip propagation associated to grain boundaries and, hence, to activate multiple slip inside the grains required to promote deformation twinning. (ii) For the present Fe–22 wt.% Mn–0.6 wt.% C TWIP steel, the effect of grain refinement within the micrometer range on the twinning stress and, hence, on twinning inhibition, is smaller than in other TWIP steels. This is supported by the experimental observation that in the present TWIP steel grain refinement within the micrometer range does not suppress twinning.

The relation (3) allows us to analyze separately the contribution of the stacking fault energy and grain size to the twinning stress. Fig. 7 shows the influence of both contributions, SFE and grain size, to the twinning stress of steel LG (average grain size of $50 \mu\text{m}$) and steel FG (average grain size of $3 \mu\text{m}$). It is seen that in both steels

Table 1

Estimated and experimental twinning stresses in a tensile deformed Fe–22 wt.% Mn–0.6 wt.% C TWIP steel with different average grain sizes.

Average grain size (μm)	$\sigma_{\text{tw}} = (1/m)(\gamma/b) + (K_{\text{tw}}^{\text{H-P}}/\sqrt{D})$ (MPa)	$\sigma_{\text{tw}} = (1/m)(\gamma/b) + (Gb/D)$ (MPa)	Experimental σ_{tw} (MPa)
50	323	274	270
3	478	290	400

the contribution of SFE to the twinning stress is larger than that of the grain size. For large grain sizes (above $50 \mu\text{m}$) the contribution of grain size to the twinning stress is small (50 MPa, less than 15% of the twinning stress), increasing its importance with grain size refinement. For an average grain size of $3 \mu\text{m}$ (steel FG) the contribution of grain size to twinning stress is similar to that of the SFE.

4.2. Effect of grain orientation

The main result concerning the influence of grain orientation on twinning behavior in the present TWIP steel tensile deformed at room temperature is that the grain orientation has a strong influence on deformation twinning at low strains but at high strains the influence decreases significantly.

The influence of grain orientation on deformation twinning is commonly explained in terms of Schmid's law for slip twin dislocations [7,15–17,29]:

$$\tau_{\text{tw}} = \sigma \cos \phi \cos \lambda \quad (7)$$

where $m = \cos \phi \cos \lambda$ is the Schmid factor, σ is the macroscopic stress in MPa, ϕ is the angle between the twinning plane normal and the tensile axis, and λ is the angle between the twinning shear direction and the tensile axis. We assume that Schmid's law is valid in the present study as in previous studies on similar TWIP steels [15], with the difference, of course, that twinning is unidirectional only. It is further assumed that the critical resolved shear stresses for both slip and twinning are approximately equal. This is supported by the strong correlation observed between slip and twinning in fcc metals, i.e. multiple slip is seen to be required for twinning to occur [9,12,29], and the results obtained in the present work showing that once multiple slip is activated twinning occurs readily resulting in similar stresses for both slip and twinning. However, this assumption does not imply that twinning can occur before slip because it is a necessary but not sufficient condition. Therefore, once multiple slip is activated, twinning occurs when the twinning stress τ_{tw} is larger than the slip stress τ_s , i.e. for those grains where the highest Schmid factor for twinning m_{tw} is larger than the highest Schmid factor for slip m_s , this is

$$m_{\text{tw}} > m_s \quad (8)$$

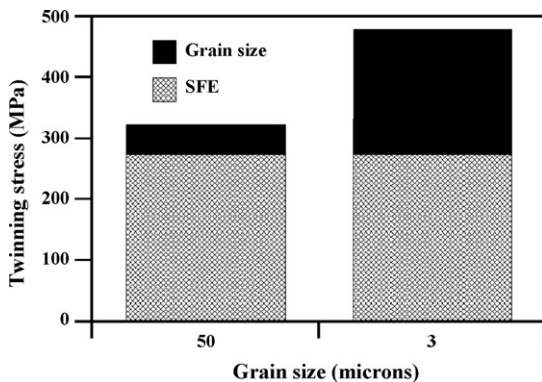


Fig. 7. Graph of the contribution of the stacking fault term (γ/b) and grain size term ($K_{\text{tw}}^{\text{H-P}}/\sqrt{D}$) on the twinning stress for steel LG (average grain $50 \mu\text{m}$) and steel FG (average grain size $3 \mu\text{m}$).

Assuming this twinning criterion, the grain orientations favorable and unfavorable for twinning can be calculated for a particular macroscopic stress. Fig. 8(a) shows the TA-IPF with calculated grain orientations favorable (red lines) and unfavorable for twinning (blue lines) during tensile deformation. The figure reveals two regions of grain orientations where twinning is favorable or not. The predicted regions are in excellent agreement with the observed grain orientations in steel LG tensile deformed to 0.05 logarithmic strain, Fig. 8(b). Almost all observed orientations fall within the corresponding Schmid regime of the TA-IPF. This result indicates first that our assumption that the critical resolved shear stresses for slip and twinning are very similar is correct. Second, Schmid's law fully explains the strong influence of grain orientation on deformation twinning observed in steel LG tensile deformed to low strain. At this strain level deformation twinning mainly occurs in grains oriented close to the $(111)/\text{TA}$ directions. Nevertheless, the Schmid law does not explain the small influence of the grain orientation on deformation twinning observed at higher

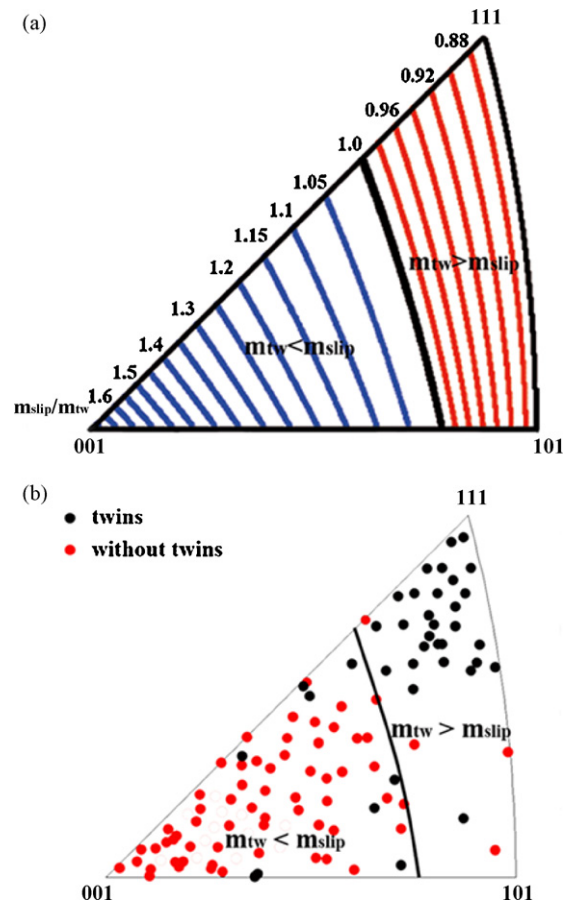


Fig. 8. (a) Inverse pole figure along tensile axis direction showing the grain orientations which are favorably (area with red lines) and unfavorably oriented (area with blue lines) for twinning according to the Schmid law and the assumption of equal critical resolved shear stresses for slip and twinning. (b) Comparison between experimental grain orientations (dots) obtained in steel LG (average grain size $50 \mu\text{m}$) tensile strained to 0.05 logarithmic strain and calculated orientation regions from the Schmid law. (For interpretation of the references to color in this figure legend, the reader is referred to the web version of the article.)

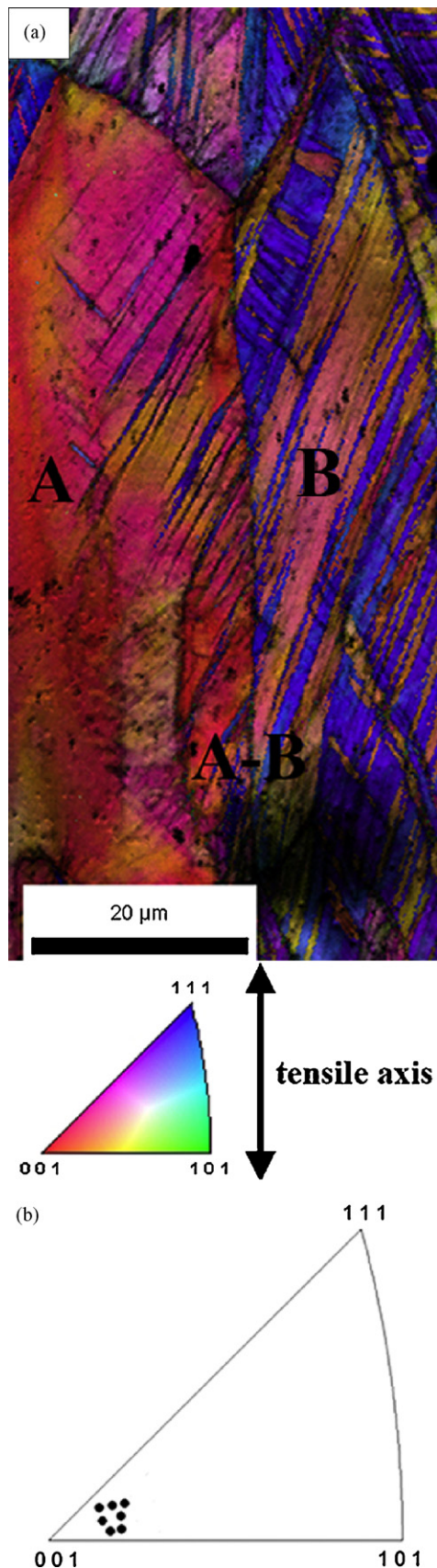


Fig. 9. (a) TA-IPF map of the steel LG (average grain size $50\ \mu\text{m}$) tensile deformed to 0.3 logarithmic strain showing a grain (grain A) that is unfavorably oriented for twinning with respect to the macroscopic stress which contains deformation twins; (b) TA-IPF of grain A (TA: tensile axis; IPF: inverse pole figure).

strain, as the TA-IPF in Fig. 6(b) shows. At 0.3 logarithmic strain, deformation twinning occurs regularly in grains oriented unfavorably for twinning according to Schmid's law taking into account the current grain orientation. Only grains oriented close to the $\langle 001 \rangle // \text{TA}$ directions are free of twins. The deviation from Schmid's law observed at high strain is not unexpected although surprisingly, it has not been reported in previous studies on TWIP steels [16,17]. This deviation can be explained as follows. The predicted orientations from Schmid's law, shown in the TA-IPF of Fig. 8(a), were calculated assuming the macroscopical unidirectional stress state to act in a similar manner everywhere in the material. In the present TWIP steel tensile deformed to high strain, the local stress state controlling deformation twinning may, however, be very different from the macroscopic one [21,32–34]. Figs. 1 and 2 reveal that the present TWIP steel develops during tensile deformation a complex and heterogeneous microstructure with a high amount of deformation twins. Deformation twins formed in one grain may create local shear stress concentrations at loci where they impinge on a grain boundary. This may lead to nucleation of twins in neighbouring grains even if they are – with respect to the macroscopic stress state – unfavorably oriented for twinning. The TA-IPF map in Fig. 9(a) shows an example of a grain unfavorably oriented for twinning with respect to the macroscopic stress which contains deformation twins (grain orientation spread is shown in the TA-IPF of Fig. 9(b)). The grain oriented close to the $\langle 001 \rangle // \text{TA}$ direction, referred to as grain A, is highly unfavorably oriented for twinning. Nevertheless, it contains a large amount of deformation twins which have, however, not grown all the way through the grain. These twins are nucleated at the grain boundary A-B where bundles of twins of the adjacent grain (grain B) impinged. A more detailed analysis on the twinning transfer across the grain boundaries would require consideration of the grain boundary character [22,34]. This has, however, not been done here.

5. Conclusions

We investigate the influence of grain size and grain orientation on deformation twinning in a tensile deformed Fe–22 wt.% Mn–0.6 wt.% C TWIP steel at room temperature. The following conclusions are drawn:

- Grain refinement within the micrometer range does not suppress deformation twinning. As deformation twins are responsible for the outstanding mechanical properties of TWIP steels, this indicates that it is feasible to tailor the mechanical properties of Fe–22 wt.% Mn–0.6 wt.% C TWIP steels with grain refinement within the micrometer range. As twinning stress is strongly dependent on the stacking fault energy, this result can not be extended to other TWIP steels as minor modifications in chemical composition may alter the stacking fault energy.
- A Hall–Petch relation $\sigma_{\text{tw}} = (\gamma/mb) + (K_{\text{tw}}^{\text{H-P}}/\sqrt{D})$ provides a good estimate of the effect of grain size within the micrometer range on the twinning stress. It was found that the Hall–Petch constant for twinning, $K_{\text{tw}}^{\text{H-P}}$, is about equal to that for slip, $K_{\text{slip}}^{\text{H-P}}$. Two significant conclusions can be drawn from this finding: (i) the effect of the grain size on twinning stress is similar to its effect on yield stress. This is ascribed to the resistance to slip propagation associated to grain boundaries. Slip propagation is associated to activation of multiple slip which is a prerequisite to deformation twin nucleation. (ii) For the present TWIP steel, the effect of grain refinement within the micrometer range on the twinning stress and, hence, on twinning inhibition, is smaller than in other TWIP steels.
- The orientation dependence of twinning at small strain shows that the critical resolved shear stress for twinning and slip are very similar as the appearance of twinning fully complies with

the Schmid law under these conditions. Deformation twinning mainly occurs in grains oriented close to $\langle 111 \rangle$ //tensile axis where the maximum resolved shear for twinning, τ_{tw} , is larger than that for slip, τ_s .

- At high strains (above 0.3 logarithmic strain), a strong deviation from the macroscopic Schmid law is observed. Deformation twins are observed in grains that are unfavourably oriented with respect to twinning according to Schmid's law. Local stress concentrations due to the accumulation of shear stresses at grain boundaries coming from incoming bundles of deformation twins, and also probably the grain boundary character, play an important role on the twinning behavior. This may lead to nucleation of twins in neighbouring grains even if they are – with respect to the macroscopic stress state – unfavourably oriented for twinning.

Acknowledgments

The authors would like to acknowledge the financial support by the German Research Foundation within the framework of the SFB 761 “steel ab initio”. The authors also acknowledge the help from Luc Hantcherli in the preparation of Fig. 8(a).

References

- [1] O. Grässel, L. Krüger, G. Frommeyer, L.W. Meyer, *Int. J. Plast.* 16 (2000) 1391–1409.
- [2] G. Frommeyer, U. Brück, P. Neumann, *ISIJ Int.* 43 (2003) 438–446.
- [3] S. Allain, J.P. Chateau, O. Bouaziz, *Mater. Sci. Eng. A* 387–389 (2004) 143–147.
- [4] S. Vercammen, B. Blanpain, B.C. De Cooman, P. Wollants, *Acta Mater.* 52 (2004) 2005–2012.
- [5] R. Ueji, N. Tsuchida, D. Terada, N. Tsuji, Y. Tanaka, A. Takemura, K. Kunishige, *Scr. Mater.* 59 (2008) 963–966.
- [6] O. Bouaziz, S. Allain, C. Scott, *Scr. Mater.* 58 (2008) 484–487.
- [7] M.N. Shiekhelsouk, V. Favier, K. Inal, M. Cherkaoui, *Int. J. Plast.* 25 (2009) 105–133.
- [8] T. Shun, C.M. Wan, J.G. Byrne, *Acta Metall. Mater.* 40 (1992) 3407–3412.
- [9] J.W. Christian, S. Mahajan, *Prog. Mater. Sci.* 39 (1995) 1–157.
- [10] J.A. Venables, *Phil. Mag.* 6 (1961) 379–396.
- [11] H. Fujita, T. Mori, *Scr. Metall.* 9 (1975) 631–636.
- [12] S. Mahajan, G.Y. Chin, *Acta Metall.* 21 (1973) 1353–1363.
- [13] N. Narita, J. Takamura, *Phil. Mag.* 29 (1974) 1001–1028.
- [14] T.H. Lee, C.S. Oh, S.J. Kim, S. Takaki, *Acta Mater.* 55 (2007) 3649–3662.
- [15] L. Bracke, L. Kestens, J. Penning, *Scr. Mater.* 61 (2009) 220–222.
- [16] P. Yang, Q. Xie, L. Meng, H. Ding, Z. Tang, *Scr. Mater.* 55 (2006) 629–631.
- [17] L. Meng, P. Yang, Q. Xie, H. Ding, Z. Tang, *Scr. Mater.* 56 (2007) 931–934.
- [18] D. Senk, H. Emmerich, J. Rezende, R. Siquieri, *Adv. Eng. Mater.* 9 (2007) 695–702.
- [19] C. Sachs, H. Fabritius, D. Raabe, *J. Struct. Biol.* 155 (2006) 409–425.
- [20] D. Raabe, M. Sachtleber, Z. Zhao, F. Roters, S. Zaefferer, *Acta Mater.* 49 (2001) 3433–3441.
- [21] D. Raabe, M. Sachtleber, H. Weiland, G. Scheele, Z. Zhao, *Acta Mater.* 51 (2003) 1539–1560.
- [22] S. Zaefferer, J.C. Kuo, Z. Zhao, M. Winning, D. Raabe, *Acta Mater.* 51 (2003) 4719–4735.
- [23] I. Gutierrez-Urrutia, S. Zaefferer, D. Raabe, *Scr. Mater.* 61 (2009) 737–740.
- [24] D. Barbier, N. Gey, S. Allain, N. Bozzolo, M. Humbert, *Mater. Sci. Eng. A* 500 (2009) 196–206.
- [25] M.A. Meyers, O. Vöhringer, V.A. Lubarda, *Acta Mater.* 49 (2001) 4025–4039.
- [26] S.G. Song, G.T. Gray III, *Metall. Mater. Trans.* 26A (1995) 2665–2675.
- [27] O. Vöhringer, *Z. Metallkd.* 67 (1976) 51.
- [28] W.Z. Han, Z.F. Zhang, S.D. Wu, S.X. Li, *Phil. Mag.* 88 (2008) 3011–3029.
- [29] I. Karaman, H. Sehitoglu, K. Gall, Y.I. Chumlyakov, H.J. Maier, *Acta Mater.* 48 (2000) 1345–1359.
- [30] G.I. Taylor, *J. Inst. Met.* 62 (1938) 307–324.
- [31] F. de las Cuevas, M. Reis, A. Ferraiuolo, G. Prato Longo, L.P. Karjalainen, J. Alkorta, J. Gil Sevillano, *Key Eng. Mater.* 423 (2010) 147–152.
- [32] Z. Zhao, M. Ramesh, D. Raabe, A. Cuitino, R. Radovitzky, *Int. J. Plast.* 24 (2008) 2278–2297.
- [33] M. Sachtleber, Z. Zhao, D. Raabe, *Mater. Sci. Eng. A* 336 (2002) 81–87.
- [34] T.R. Bieler, P. Eisenlohr, F. Roters, D. Kumar, D.E. Mason, M.A. Crimp, D. Raabe, *Int. J. Plast.* 25 (2009) 1655–1683.

Dislocation and twin substructure evolution during strain hardening of an Fe–22 wt.% Mn–0.6 wt.% C TWIP steel observed by electron channeling contrast imaging

I. Gutierrez-Urrutia*, D. Raabe

Max-Planck-Institut für Eisenforschung, Max-Planck Str. 1, D-40237 Düsseldorf, Germany

Received 11 March 2011; received in revised form 3 July 2011; accepted 4 July 2011

Available online 29 July 2011

Abstract

We study the kinetics of the substructure evolution and its correspondence to the strain hardening evolution of an Fe–22 wt.% Mn–0.6 wt.% C TWIP steel during tensile deformation by means of electron channeling contrast imaging (ECCI) combined with electron backscatter diffraction (EBSD). The contribution of twin and dislocation substructures to strain hardening is evaluated in terms of a dislocation mean free path approach involving several microstructure parameters, such as the characteristic average twin spacing and the dislocation substructure size. The analysis reveals that at the early stages of deformation (strain below 0.1 true strain) the dislocation substructure provides a high strain hardening rate with hardening coefficients of about $G/40$ (G is the shear modulus). At intermediate strains (below 0.3 true strain), the dislocation mean free path refinement due to deformation twinning results in a high strain rate with a hardening coefficient of about $G/30$. Finally, at high strains (above 0.4 true strain), the limited further refinement of the dislocation and twin substructures reduces the capability for trapping more dislocations inside the microstructure and, hence, the strain hardening decreases. Grains forming dislocation cells develop a self-organized and dynamically refined dislocation cell structure which follows the similitude principle but with a smaller similitude constant than that found in medium to high stacking fault energy alloys. We attribute this difference to the influence of the stacking fault energy on the mechanism of cell formation.

© 2011 Acta Materialia Inc. Published by Elsevier Ltd. All rights reserved.

Keywords: Strain hardening; Electron channeling contrast imaging; Austenitic steel; Dislocation structures; Deformation twinning

1. Introduction

High-manganese steels have received much interest in recent years due to their outstanding mechanical properties combining high strength and ductility. This property profile is attributed to their high strain hardening capacity. High-manganese steels are typically austenitic steels, i.e. face-centered cubic (fcc) alloys, with a high Mn content (above 20% wt.%) and additions of elements such as carbon (<1 wt.%), silicon (<3 wt.%) and aluminum (<10 wt.%). This steel grade exhibit different hardening mechanisms, such as transformation-induced plasticity

(TRIP) [1,2], twinning-induced plasticity (TWIP) [1,3–8] or microband-induced plasticity (MBIP) [9,10]. The activation of these mechanisms is strongly dependent on the stacking fault energy. TRIP is observed in very low stacking fault steels (below 20 mJ m^{-2}) and is associated with the transformation of austenite (fcc phase) into ϵ -martensite (hexagonal close-packed phase), which in turn further acts as nucleus of α' -martensite (body-centered cubic or tetragonal phase) [11,12]. TWIP is observed in medium stacking fault energy steels ($20\text{--}40 \text{ mJ m}^{-2}$) and is characterized by the formation of deformation twins with nanometer thickness. MBIP has been recently reported in steel grades with high stacking fault energy ($\sim 90 \text{ mJ m}^{-2}$) and is attributed to the formation of microbands, which are in-grain shear zones that are confined by geometrically nec-

* Corresponding author. Tel.: +49 2116792 211; fax: +49 2115792333.

E-mail address: i.gutierrez@mpie.de (I. Gutierrez-Urrutia).

essary boundaries or conventional grain boundaries. These microstructure features (ϵ -martensite plates, deformation twins and microbands) lead to a remarkable variety of strain hardening phenomena as they all act as effective obstacles for dislocation glide. High-manganese TWIP steels are characterized by a hierarchical microstructure refinement that includes complex dislocation and twin substructures, and their interactions. Although there are some previous studies on the strain hardening behavior in TWIP steels, the details of the underlying kinetics of the substructure evolution and its correspondence to the stress–strain and strain hardening evolution is not yet fully understood. Most of these works analyze strain hardening in terms of a dislocation mean free path (MFP) approach, focusing essentially on a single microstructure parameter, namely, the twin spacing [3,13–17]. These works attribute the high strain hardening rate at intermediate strains (0.1–0.2 true strain) to twin spacing refinement. The increasing density of deformation twin boundaries and the strong effect they have on dislocation glide leads to the so-called “dynamic Hall–Petch effect”. However, our analysis reveals that the deformed microstructure of these alloys is too complicated to be reduced to a single microstructure parameter and, therefore, a detailed analysis of the contribution of dislocation and twin substructures, as well as their interactions, to strain hardening is required.

One important limitation in the characterization of TWIP steels is the complexity of the microstructure, which involves features of different length scales: deformation twins with thicknesses of some tens of nanometers [3,16,18] and dislocation substructures extending over several micrometers. As a consequence of this scale discrepancy, quantitative microstructure characterization by conventional electron microscopy techniques such as electron backscatter diffraction (EBSD) or transmission electron microscopy (TEM) is limited due to the angular resolution (EBSD) and the small field of view (TEM), respectively. In this study, therefore, we make use of electron channeling contrast imaging (ECCI), which is conducted in a scanning electron microscope (SEM), to perform a quantitative characterization of the deformation microstructure of TWIP steel. The ECCI technique has been established as an excellent tool for examining complex deformation microstructures of metallic materials, revealing microstructure features such as deformation twins, stacking faults and complex dislocation arrangements from a wide field of view directly in the SEM [6,19–25]. The reason for the recent improvement in the ECCI technique lies in its combination with EBSD. This allows us to efficiently identify optimum contrast conditions and, therefore, produce ECCI images of crystal defects under controlled diffraction conditions [24].

The present study aims at understanding the strain hardening behavior of an Fe22 wt.% Mn–0.6 wt.% C TWIP steel through a complete quantitative characterization of the dislocation and twin substructure evolution via an EBSD-optimized ECCI approach. The contribution of

the so-characterized substructure to the strain hardening is analyzed in terms of the dislocation mean free path approach involving several microstructure parameters, such as the characteristic average twin spacing and the dislocation substructure length scale.

2. Experimental

The TWIP steel used in this study had the chemical composition Fe–22 wt.% Mn–0.6 wt.% C. The material was melted in an induction furnace under an Ar atmosphere and cast into round bars of 25 mm diameter. To avoid Mn segregation [26], samples were swaged to 20% area reduction at 1000 °C and subsequently solution-treated for 4 h at 1100 °C under Ar. Thereafter, samples were hot-rolled to 75% engineering thickness at 1000 °C followed by air cooling. The hot-rolled material showed a fully austenitic structure with an average grain size of 50 μm , which remained stable during deformation at room temperature.

Tensile tests were carried out at room temperature at an initial strain rate of $5 \times 10^{-4} \text{ s}^{-1}$. In addition to tensile testing to failure, interrupted tensile tests to true strains of $\epsilon = 0.05, 0.10, 0.30$ and 0.40 were performed to study the microstructural evolution as a function of strain. The tensile bone-shaped samples had an 8 mm gage length, 2 mm gage width and 1 mm gage thickness. The monotonic tensile deformation experiments were carried out on a tensile test instrument (Kammrath & Weiss GmbH, Dortmund, Germany) equipped with a digital image correlation (DIC) system (ARAMIS system, GOM-Gesellschaft für Optische Messtechnik mbH, 38106 Braunschweig, Germany) to measure the local and macroscopic strain distribution. Details of this set-up are described in Ref. [27]. The surface pattern required for DIC was obtained as explained in Ref. [6]. Averaged engineering strain values were retrieved from the corresponding strain maps and used to calculate the true stress–strain values.

Microstructures of the tensile deformed TWIP steel were examined by two types of scanning electron microscopy techniques, namely, electron back scatter diffraction (EBSD) and electron channeling contrast imaging (ECCI). The EBSD technique was used to analyze the local crystallographic texture together with the dislocation and twin substructure. Orientation maps were taken in a 6500 F JEOL field emission gun-scanning electron microscope equipped with a TSL OIM EBSD system at 15 kV acceleration voltage and with a working distance of 15 mm. EBSD maps are displayed as inverse pole figure (IPF) maps in the direction of the tensile axis (TA). The ECCI technique was used to image deformation twins and dislocation substructures, as introduced in a previous work on TWIP steels [6]. A recently reported new set-up for ECCI [24] was used in this study to obtain ECCI images under controlled diffraction conditions, enabling an enhanced dislocation and interface contrast. The set-up makes use of the EBSD technique for orienting the crystal into optimal diffraction con-

ditions. ECCI images were obtained with optimum contrast by orienting the matrix crystal exactly in the Bragg condition for a high-intensity reflection and exciting the corresponding diffraction vector in a “two-beam” condition. ECCI observations were carried out in a Zeiss Cross-beam instrument (XB 1540; Carl Zeiss SMT AG, Germany) consisting of a Gemini-type field emission gun electron column and a focused ion beam device (Orsay Physics). ECCI was performed at 10 kV acceleration voltage and a working distance of 6 mm, using a solid-state four-quadrant BSE detector. The microscope was run in the “high current” mode and an objective lens aperture of 120 μm was used.

3. Results

3.1. Strain hardening

Fig. 1 shows a set of true stress–strain curves of the Fe–22 wt.% Mn–0.6 wt.% C TWIP steel tensile deformed at a strain rate of $5 \times 10^{-4} \text{ s}^{-1}$. We include here both the complete and interrupted tensile tests. The TWIP steel exhibits excellent mechanical properties, combining high strength (ultimate tensile strength of 1.1 GPa) and ductility (elongation to failure of 50%). It is important to note that between 0.1 and 0.2 true strain the stress–strain curve assumes a slightly concave shape, i.e. at this strain level secondary strain hardening effects seem to occur.

Fig. 2 shows the normalized strain hardening rate (normalized by the shear modulus) vs. flow stress (a) and true strain (b) of the tensile deformed material. Arrows indicate the different deformation stages described in the subsequent section. The main features revealed in Fig. 2 are, first, the remarkably high overall strain hardening rate and, second, the fact that the curve reveals a minimum at intermediate strains (0.06–0.1 true strain). This hardening

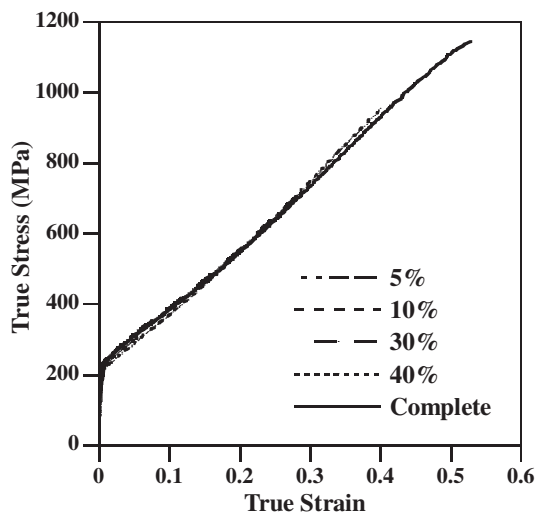


Fig. 1. True stress–true strain curves of Fe–22 wt.% Mn–0.6 wt.% C TWIP steel corresponding to interrupted and complete (i.e. until rupture) tensile tests. Initial strain rate: $5 \times 10^{-4} \text{ s}^{-1}$.

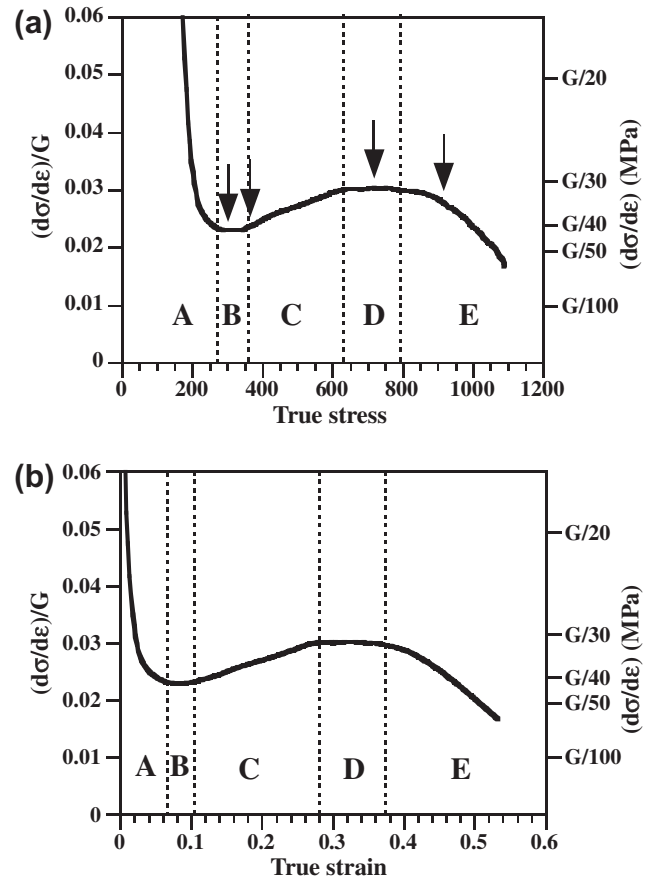


Fig. 2. Normalized strain hardening rate (normalized by the shear modulus) vs. true stress (a) and true strain (b) of tensile deformed Fe–22 wt.% Mn–0.6 wt.% C TWIP steel.

stage is followed by a high strain hardening rate at higher deformations. Typically, structural metallic alloys reveal a monotonous decay of the strain hardening rate as a function of strain. More specifically, in the current study five different deformation stages can be clearly distinguished in the evolution of the strain hardening rate with the true stress. The first stage, referred to as stage A, is characterized by a continuous decrease in the strain hardening rate until 270 MPa. This stage is similar to the stage III hardening regime of fcc metals with high stacking fault energy, such as copper and aluminum [28]. At this stress level, the strain hardening coefficient is about $G/40$, where G is the shear modulus. The hardening rate remains almost constant with a strain hardening coefficient of about $G/40$ during a small stress increment until 360 MPa (stage B). With increasing stress, the strain hardening rate increases gradually, reaching a strain hardening coefficient of about $G/30$ at 630 MPa (stage C). With further stress, the strain hardening rate is nearly constant, with a strain hardening coefficient of about $G/30$ up to a stress level of 800 MPa (stage D). Finally, the strain hardening rate decreases until rupture (stage E). It should be pointed out that the labeling of the hardening stages used in this work must not be confused with the classical hardening stage analysis used for

single crystals and polycrystals, which does not reveal a minimum in strain hardening after the classical stage III hardening regime.

3.2. Texture evolution

In its initial hot-rolled and homogenized state the material showed a fully austenitic structure, which remained stable during deformation at room temperature. No evidence of ϵ -martensite was detected by EBSD on the tensile deformed samples. Fig. 3 shows the texture evolution of the TWIP steel during tensile deformation. Fig. 3a shows the IPF for the crystal direction along the TA of the initial material, revealing a weak texture before the tensile test. Fig. 3b–e shows the textures in terms of TA-IPFs of the steel deformed to 0.05, 0.10, 0.30 and 0.40 true strain, respectively. We observe that the texture sharpens slightly during tensile deformation. At 0.3 true strain, the texture is characterized by two strong components, namely $\langle 111 \rangle // \text{TA}$ and $\langle 001 \rangle // \text{TA}$, which both remain stable

and sharpen slightly further during the ongoing deformation. Similar textures have been previously observed in tensile deformed TWIP steels at room temperature [16,29].

3.3. Evolution of the dislocation and twin substructure

At the early stage of deformation (strain below a true strain of 0.1), the microstructure mainly consists of dislocation substructures, with very few deformation twins. In this regime, the twinned area fraction is about 0.001 (Fig. 4a and b). Parts (a) and (b) of the figure show ECCI images of deformed microstructures of TWIP steels at 0.05 true strain/310 MPa and 0.1 true strain/380 MPa, respectively. These stress levels fall into stage B of strain hardening. The micrographs reveal that less than 20% of all grains contain deformation twins, which are mainly distributed along a single active twinning system (the primary twin system). At this stage of deformation, planar arrangements of dislocations consisting of dense dislocation layers forming on planes corresponding to the most active slip systems

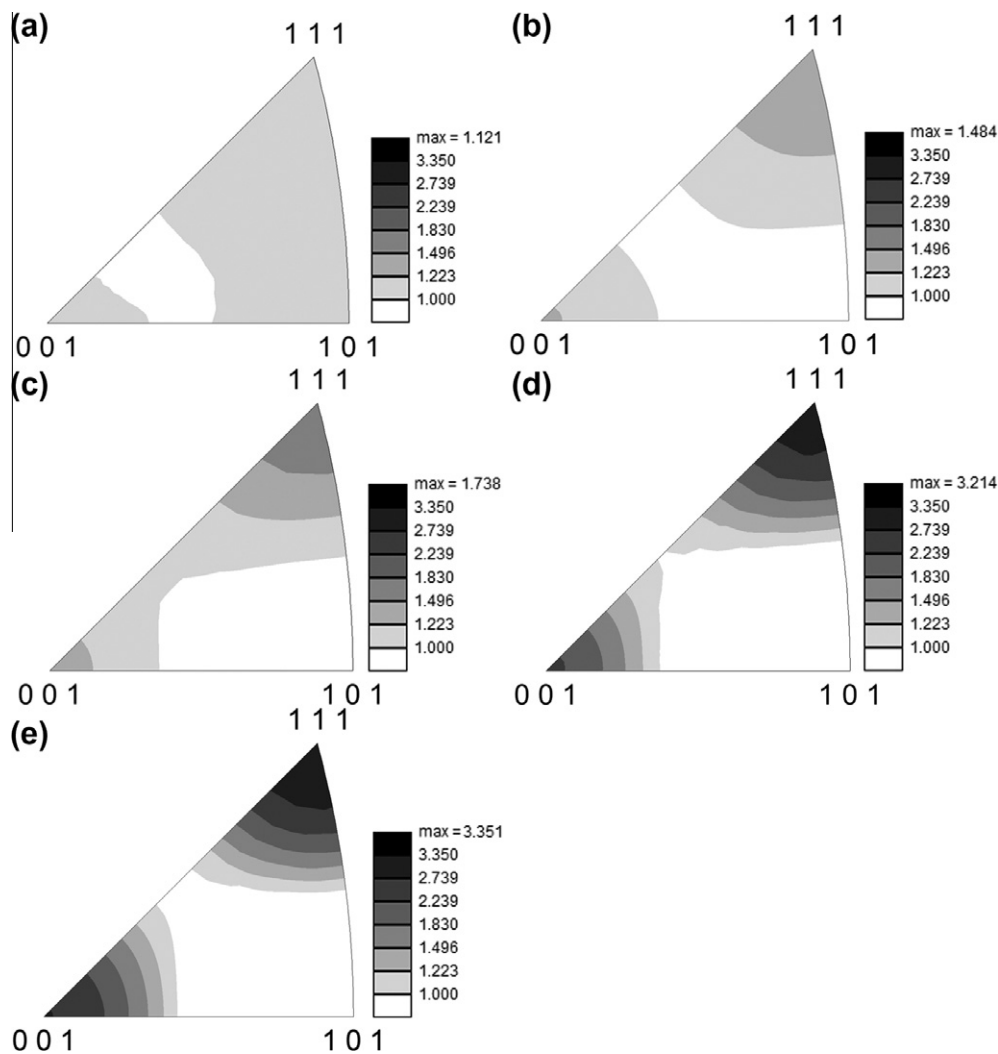


Fig. 3. IPFs along the TA direction of Fe–22 wt.% Mn–0.6 wt.% C TWIP steel in different states: as hot-rolled (a); tensile deformed to 0.05 true strain (b); 0.1 true strain (c); 0.3 true strain (d); 0.4 true strain (e).

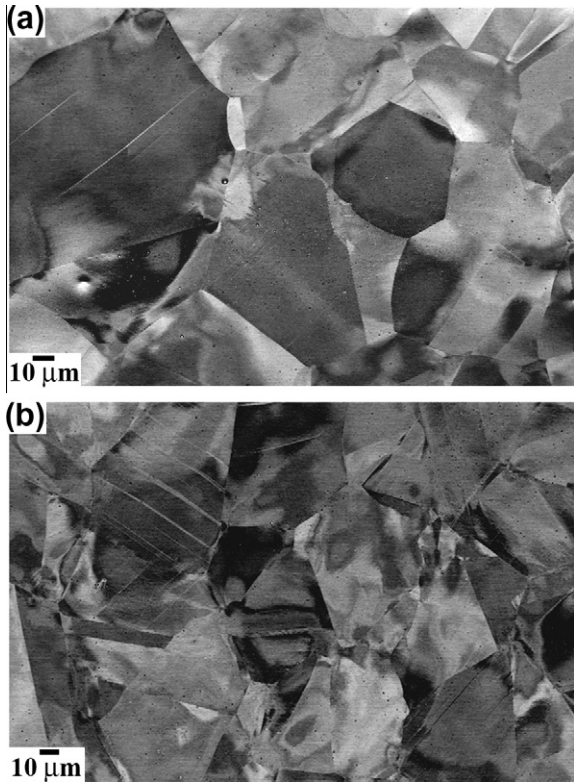


Fig. 4. ECCI images of deformed microstructures at 0.05 true strain (a) and 0.1 true strain (b), respectively.

are visible, as illustrated in the ECCI image in Fig. 5a. These dislocation substructures are referred to as highly dense dislocation walls (HDDWs) [30–32]. HDDWs are dislocation boundaries with a high dislocation density and a rotational component separating regions with different combinations of simultaneously operating glide systems. HDDWs appear in the ECCI images under the corresponding Bragg condition as bright straight compact layers penetrating the whole grain. This dislocation pattern is similar to that obtained in bright-field TEM images of HDDWs in medium-to-high stacking fault energy metals [30,31]. However, the contrast in ECCI imaging is reverted compared to that obtained in bright-field TEM due to the electron channeling mechanism and the diffraction conditions used to image dislocation substructures. In particular, Fig. 5a shows an example of HDDWs formed along the $(-1\ 1\ -1)$ slip plane on a sample that was tensile deformed to 0.05 true strain. The ECCI-based slip trace analysis was conducted by an accompanying EBSD map in the same area. HDDWs have been observed in medium-to-high stacking fault energy metals [30,31] as well as in low stacking fault energy alloys [33,34].

With further straining (to 0.1 true strain), a heterogeneous dislocation substructure is formed due to the multiple character of slip (planar and wavy), as illustrated in Fig. 5b. Planar slip promotes the formation of structures created by the intersection of HDDWs on two different slip planes, referred to as HDDW structures. These intersec-

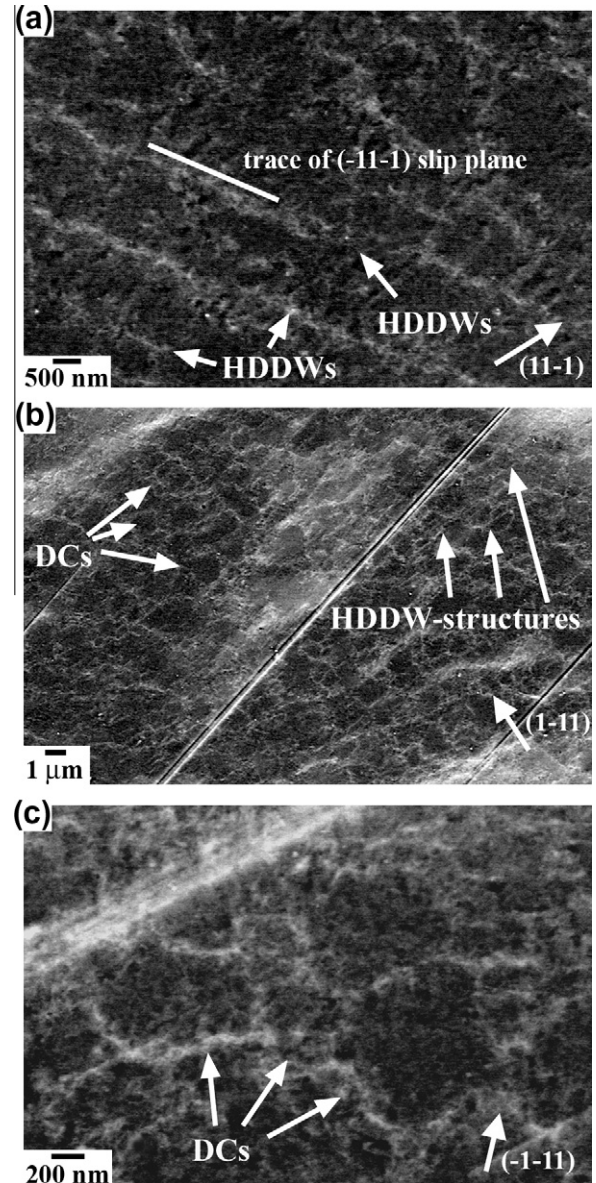


Fig. 5. ECCI images of deformed microstructure at the early stages of deformation (strain below 0.1 true strain). (a) HDDWs along the $(-1\ 1\ -1)$ slip plane on a sample tensile deformed to 0.05 true strain. The ECCI image was obtained by orienting the grain into Bragg condition using the $(1\ 1\ -1)g$ vector (arrow). (b) DCs and HDDW structures in a sample tensile deformed to 0.1 true strain. The ECCI image was obtained by orienting the grain into Bragg condition using the $(1\ -1\ 1)g$ vector (arrow). (c) Details of the DC structure on a sample tensile deformed to 0.05 true strain. The ECCI image was obtained by orienting the grain into Bragg condition using the $(-1\ -1\ 1)g$ vector (arrow).

tions lead to a checkerboard-type pattern, which is commonly observed in low stacking fault energy metals [33,34]. Wavy slip promotes the formation of equiaxed dislocation cells (DCs) similar to those observed in medium-to-high stacking fault energy metals [30,32]. These dislocation substructures appear in ECCI images under the current diffraction conditions as bright globular structures with a sharp boundary contrast. This dislocation pattern is similar to that obtained in bright-field TEM, as shown

in a previous work [24]. As discussed before, the contrast in ECCI is reverted to that in bright-field TEM due to the electron channeling mechanism and the diffraction conditions used to image dislocation substructures. The ECCI image shown in Fig. 5c reveals in detail dislocation cells with sizes ranging between 500 and 1000 nm formed at 0.05 true strain. At this strain, the average size of the dislocation substructure (both HDDW structures and DCs) is 750 nm. With further strain (0.1 true strain), the dislocation substructure is refined to an average size of 650 nm.

At a true strain of 0.3, the twinning activity increases remarkably, leading to the development of a well-defined twin substructure. At this stage, most of the grains contain deformation twins that are active in several systems (up to three twinning systems in the same grain are observed), and only around 10% of the grains are free of deformation twins. With further straining, the twin activity increases slightly. Fig. 6a and b shows ECCI images of the twin substructure formed at 0.3 true strain/720 MPa (stage D of strain hardening) and 0.4 true strain/920 MPa (stage E of strain hardening), respectively. These images show the formation of a well-defined twin substructure that penetrates the grains and subgrains. These crystals have sizes in the range between 10 and 40 μm . It can be also seen that even at high strains some grain regions remain free of deformation twins. At this stage (0.3–0.4 true strain), we can systematically distinguish three types of grains/subgrains according to the twin substructure occurring in them: type

I grains, which are characterized by a low deformation twinning activity; type II grains, which contain a well-developed twin substructure along one active twinning system (the primary twin system according to the highest Schmid factor); and type III grains, which build up a well-developed twin substructure along more than one active twinning system (primary and secondary twin systems). We define primary twin systems as those systems with the highest Schmid factor. The other twin systems are referred to as secondary twin systems. The evolution of the grain area fraction, the average size of dislocation substructures and the average twin spacing of each type of grain are shown in Table 1.

3.4. Orientation dependence of the dislocation and twin substructure

The grain orientation dependence of the twin substructure was analyzed via EBSD mapping in 150 individual grains/subgrains of a sample tensile deformed to 0.3 true strain. About 10 regions were characterized for each grain/subgrain. The average orientation is plotted in the TA-IPF of Fig. 7, with red, green and blue dots corresponding to type I, II and III grains, respectively. The data reveal that the different types of twin substructures observed are characteristic of specific orientation components: type I grains (low twinning activity) are oriented close to $\langle 001 \rangle // \text{TA}$ directions within an angular range of approximately 15° ; type II grains (primary twin system active) are oriented along the line between $\langle 001 \rangle // \text{TA}$ and $\langle 111 \rangle // \text{TA}$ directions; and type III grains (primary and secondary twin systems active) are oriented close to $\langle 111 \rangle // \text{TA}$ directions within an angular range of approximately 15° .

Figs. 8–10 show ECCI images of type I, II and III grains, respectively. Type I grains occur less frequently with an area fraction of about 10%. These grains/subgrains are oriented close to $\langle 001 \rangle // \text{TA}$ directions and exhibit low deformation twinning activity, as is evident from the small amount of twin bundles (Fig. 8a). These bundles are nucleated at grain boundaries and do not extend further up to the opposite grain boundary, but they only grow a few microns into the grain interior without impinging on other interfaces. Type I grains contain a fine equiaxed dislocation cell structure, with an average cell size of 220 nm at 0.3 true strain (Fig. 8b). Further straining (0.4 true strain) leads to a slight refinement of the cell size to an average value of 180 nm. Type II grains, with an area fraction of about 30%, exhibit significant deformation twinning activity. These grains/subgrains are oriented along the line between the $\langle 001 \rangle // \text{TA}$ and $\langle 111 \rangle // \text{TA}$ crystallographic directions. They contain a lamellar twin structure along a primary twinning system, as shown in Fig. 9a. At 0.3 true strain, the average twin spacing is 320 ± 50 nm, which is slightly reduced to 280 ± 50 nm with increasing deformation to 0.4 true strain. Fig. 9b shows that the lamellar twin structure is formed by single deformation twins, with a

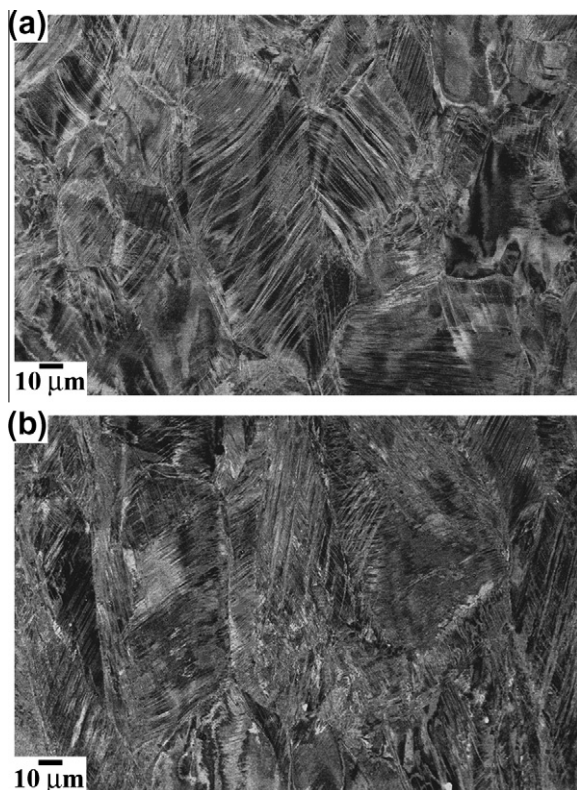


Fig. 6. ECCI images of deformation microstructures at 0.3 true strain (a) and 0.4 true strain (b), respectively.

Table 1

Evolution of the grain area fraction, the average size of dislocation substructures, and the average twin spacing with true strain/stress in type I, II and III grains. Type I grains: equiaxed cell structure with a low deformation twinning activity; type II grains: well-developed twin substructure along one active twinning system (primary twin system); type III grains: dislocation cells and highly-dense dislocation walls-structures with a well-developed twin substructure along more than one active twinning system (primary and secondary twin systems) (see also Figs. 7 and 15).

True strain	True stress (MPa)	Type I		Type II		Type III		
		Area fraction (%)	Dislocation substructure size (nm)	Area fraction (%)	Twin spacing (nm)	Area fraction (%)	Twin spacing (nm)	Dislocation substructure size (nm)
0.05	310	100	750 ± 150	0	–	0	–	–
0.1	380	~100	650 ± 100	0	–	0	–	–
0.3	720	10	220 ± 50	30	320 ± 50	60	430 ± 100	550 ± 100
0.4	920	10	180 ± 50	30	280 ± 50	60	260 ± 50	450 ± 100

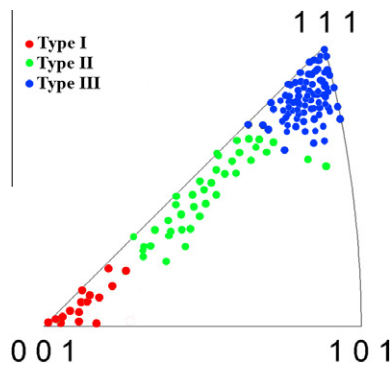


Fig. 7. IPFs along the TA direction showing experimental grain orientations of a sample deformed to 0.3 true strain with red, green and blue dots corresponding to type I, II and III grains, respectively. The classification indicates basic differences in the dislocation cell and twinning substructures developed in the different grains: type I grains: equiaxed cell structure with a low deformation twinning activity; type II grains: well-developed twin substructure mainly along one active twinning system (primary twin system: system with highest Schmid factor); type III grains: DCs and HDDW structures with a well-developed twin substructure along more than one active twinning system (primary and secondary twin systems) (see also Fig. 15 and Table 1).

thickness distribution ranging from 30 to 100 nm. At 0.3–0.4 true strain, the average twin thickness is 80 ± 20 nm. True twin thicknesses and spacings were determined by ECCI observations at high magnification for a set of about 500 deformation twins under diffraction conditions with a $\{111\}$ plane reflector parallel to the twin interface, i.e. the twins were monitored in edge-on position. Fig. 9a and b reveals that twin boundaries cut through the existing dislocation substructure developed during the early stages of deformation (HDDW structures and DCs) without experiencing strong resistance. As a consequence, a new block-shaped nanostructure is formed, as revealed in Fig. 9b. This nanostructure consists of twin boundaries along the active twin system and dislocation walls (HDDWs or cell walls) formed along the most active slip systems. The average size of the blocky nanostructure can be roughly estimated as the twin spacing times the cell size,

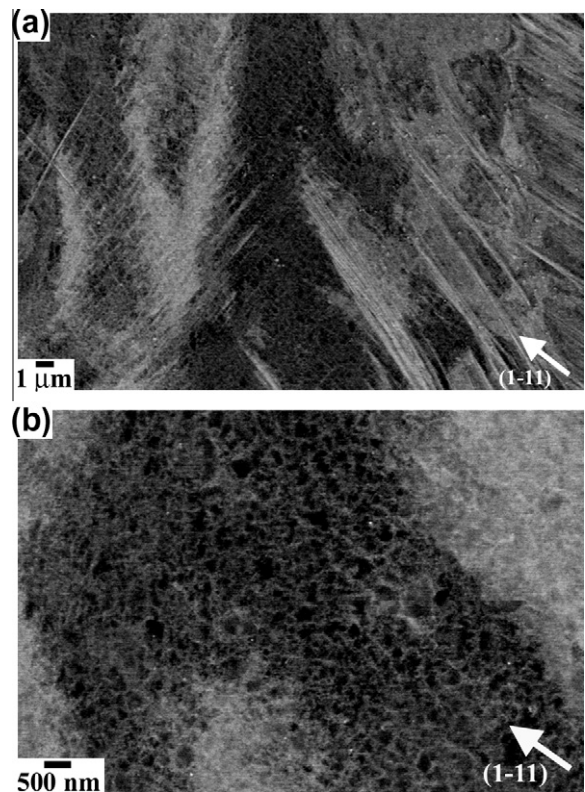


Fig. 8. ECCI images of deformation microstructure of a type I grain at 0.3 true strain. ECCI images were obtained by orienting the grain into Bragg condition using the $(1-11)g$ vector (arrow). (a) Large field of view image showing dislocation cells and bundles of twins. (b) Details of the dislocation cell structure.

which is about $300 \text{ nm} \times 500 \text{ nm}$ in the 0.3–0.4 true strain regime. Type III grains are the most frequently occurring grains, with an area fraction of 60%. These grains are oriented close to $\langle 111 \rangle // \text{TA}$ directions and exhibit a significant deformation twinning and dislocation activity. The twinning activity results in a well-defined twin substructure consisting of a primary twin system and one or two secondary twin systems (Fig. 10a). Deformation twins are typically arranged in bundles with thicknesses between 80 and 450 nm. Thin deformation twins with a thickness

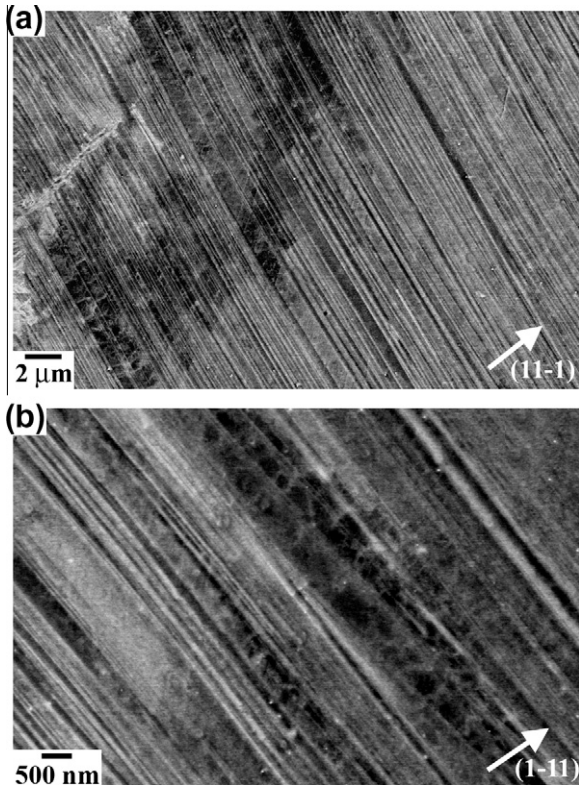


Fig. 9. ECCI images of deformation microstructure of a type II grain at 0.3 true strain. (a) Large field of view image showing a lamellar twin structure. The ECCI image was obtained by orienting the grain into Bragg condition using the $(1\ 1\ -1)g$ vector (arrow). (b) Details of the lamellar twin structure. Dislocation boundaries are visible in areas with large twin spacing. The ECCI image was obtained by orienting the grain into Bragg condition using the $(1\ -1\ 1)g$ vector (arrow).

between 20 and 60 nm are only observed on secondary twin systems, as illustrated in Fig. 10b. Apparent twin thicknesses were measured from ECCI images and corrected values were then determined by means of a stereological correction considering the corresponding tilting conditions. Fig. 10a and b reveals that these crystals contain a refined dislocation substructure, consisting of HDDW structures and DCs with an average size of 550 nm at 0.3 true strain. With further deformation (0.4 true strain), the structure is refined to an average value of 450 nm. Fig. 10 also reveals that the dislocation–twin interaction is similar to that occurring in type II grains. As a consequence, a rhomboid-shaped nanostructure of twin boundaries and dislocation walls (HDDWs or cell walls) is formed. The evolution of this nanostructure is further favored by twin–twin intersections due to the activation of multiple twin systems.

4. Discussion

4.1. Evolution of the dislocation and twin substructure

Two important aspects of the substructure evolution during tensile testing are quantitatively examined in this study, namely the dislocation and twin substructures. As

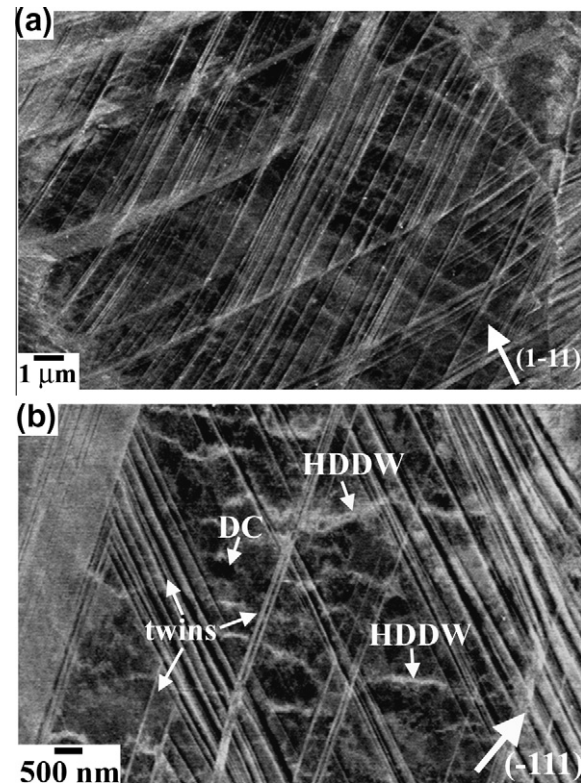


Fig. 10. ECCI images of deformation microstructure of a type III grain at 0.3 true strain. (a) Large field of view image showing a multiple twin structure with dislocation substructures. The ECCI image was obtained by orienting the grain into Bragg condition using the $(1\ -1\ 1)g$ vector (arrow). (b) Details of the dislocation substructure consisting of HDDWs and DCs. The ECCI image was obtained by orienting the grain into Bragg condition using the $(-1\ 1\ 1)g$ vector (arrow).

the ECCI images quantitatively reveal, during the early stages of deformation (strain below 0.1 true strain) the deformed microstructure is formed by DCs and highly dense dislocation arrangements (HDDWs and HDDW structures). ECCI images reveal dislocation patterns that are similar to those found in TEM observations on dislocation substructures in low-to-medium stacking fault energy metals [30–33]. In particular, the characteristic dislocation cell pattern observed by ECCI in the present FeMn alloy was confirmed by TEM in a previous work [24]. The dislocation substructures can be classified according to the character of the observed slip patterns, namely wavy or planar. The planar slip character in fcc metals is known to be mainly promoted by decreasing stacking fault energy, increasing friction stress and the occurrence of short-range ordering [35,36]. In the present TWIP steel, where ordering has not been observed, the two parameters that can promote planar slip are predominantly the friction stress ($\sigma_0 = 157$ MPa [17], which is higher than for materials exhibiting planar slip such as stainless steels [37,38]) and the stacking fault energy (22 mJ m^{-2} [39]). The latter effect promotes slip via Shockley partial dislocations. These can only cross-slip after stress- and thermally assisted local recombination, hence the planar slip prevalence in

materials with low stacking fault energy. With increasing strain (strain above 0.3 true strain), planar dislocation structures are further developed in grains that are characterized by a limited number of active slip systems, i.e. type II and III grains. Wavy dislocation structures are promoted in grains when a high number of slip planes are activated and dislocation cross-slip is enabled [30,40], such as in type I grains. Interestingly, in high stacking fault energy metals, such as pure aluminum, a similar crystallographic orientation dependence of the dislocation substructure was observed, as in the present Fe–Mn alloy [41]. This finding suggests that dislocation cell formation is promoted in similar crystal orientations in both low and high stacking fault energy metals, although the characteristic mechanism of cell formation may well be different, as discussed below. Regarding the formation of HDDWs in type III grains, the slip trace analysis conducted in 10 grains through combined ECCI and EBSD analysis reveals that most of the HDDWs are boundaries with a specific crystallographic orientation. Fig. 11a shows an example of HDDWs lying along two slip systems. The simulated diffraction pattern of the crystallographic orientation obtained from EBSD is shown in Fig. 11b. The grain is oriented close to the $(3 -1 -2)$ direction. Trace analysis reveals that the two sets

of HDDWs are formed with a specific crystallographic orientation. One set of HDDWs is formed along the $(1 -1 1)$ slip plane. The other set is formed along the $(1 -1 -1)$ slip plane within a range of 10° . The present observations on HDDWs agree with previous results obtained in low stacking fault energy alloys, such as Hadfield steel [33,34]. Our result suggests that in type III grains there are two active slip systems in the same slip plane that account for a large fraction of the total slip in the respective crystal [42].

In a previous work [6], we have shown that in the present alloy, when tensile deformed to a high true strain of 0.3, only grains with either a highly favorable or unfavorable orientation for twinning follow the Schmid behavior. These grains correspond to crystals oriented close to the $\langle 1 1 1 \rangle // TA$ and $\langle 0 0 1 \rangle // TA$ directions, respectively. This result indicates that in the present twin substructure only type III and I grains follow the Schmid behavior. The rest of the crystals, viz. type II grains with a lamellar twin structure, do not fulfill Schmid's law when considering the macroscopic load. We also observe that local stress concentrations at grain boundaries (e.g. those caused by the impingement of deformation twins formed in a neighboring grain on a grain boundary) can promote twinning in unfavorably oriented grains. These stresses can be high enough to activate the twin system with the highest Schmid factor (primary twin system). The developed twin substructure may hinder the growth of deformation twins on secondary twin systems because the stress required to build up a secondary twin substructure is probably too high to be attained during tensile deformation. As a consequence, only primary deformation twin is activated, resulting in a lamellar twin structure. This effect is similar to the well-known effect of overshooting in slip due to latent hardening.

It is worth noting the relatively small mechanical resistance that dislocation boundaries (cell walls and HDDWs) have against twin boundaries that cut through them. If we consider that the interaction is stress controlled, this observation indicates that dislocation boundaries have a small influence on the stress required for twin dislocations to pass through them. This is supported by the fact that mechanical twins, once nucleated, practically always penetrate grains to the opposite grain boundary. This behavior can be discussed in terms of the self-stresses that characterize the leading twin edge. Mechanical twins in fcc metals are formed by the passage of edge-type Shockley partial dislocations on successive twinning planes. These partials form inclined arrays at the twin–matrix interface. Therefore, a twin can be described by a field of discrete partial dislocations where the long-range field resembles that of a pile-up configuration of partials [43–45]. Kamat et al. [44] have shown that under usual deformation conditions a twin resembles a discontinuous tilt wall formed by inclined pile-ups. This means that a growing twin can be considered as a coordinated movement of partial dislocations that preserve their characteristic arrangement. The partial dislocations in this array are spaced by a value of h (Fig. 12a). The

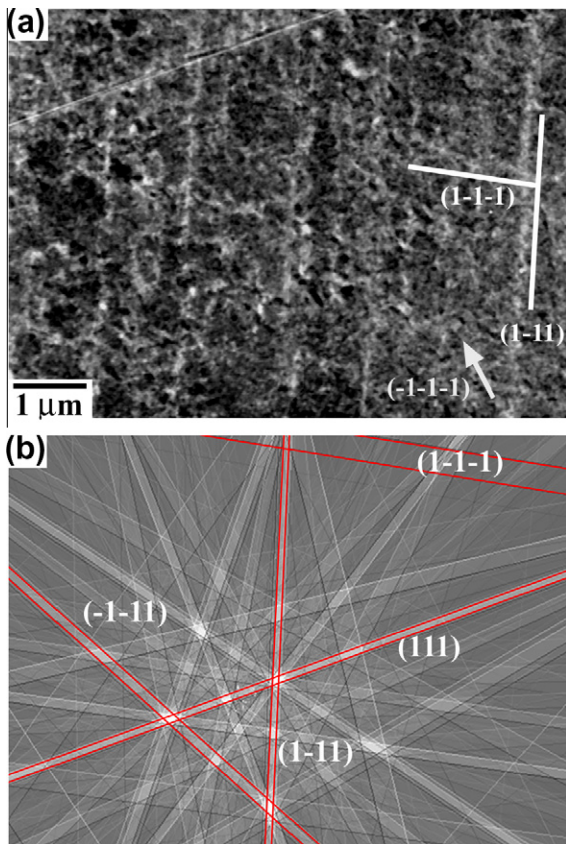


Fig. 11. Trace analysis of the crystallographic orientation of the alignment of HDDWs by using a combination of ECCI and EBSD. (a) ECCI image of HDDWs. (b) Simulated diffraction pattern of the corresponding crystal orientation. The crystal orientation is close to the $(3 -1 -2)$ direction//TA.

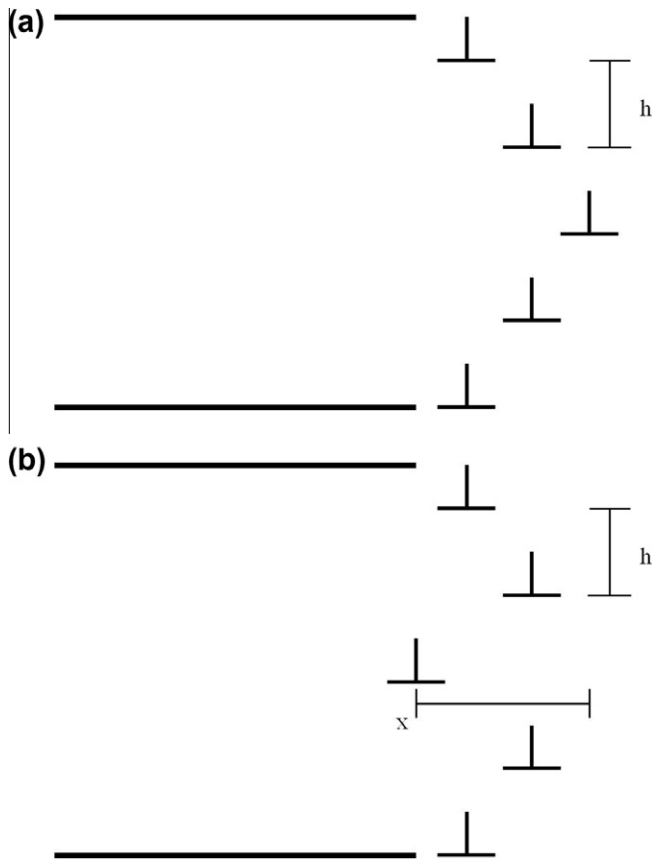


Fig. 12. Schematic representation of the leading edge of a deformation twin formed by a set of Shockley partials separated by distance h . (a) Twin tip in local mechanical equilibrium. (b) Twin tip out of local mechanical equilibrium with the leading partial dislocation being retarded and displaced by x . The local Peach–Koehler forces on this dislocation are in the GPa range, so the local mechanical equilibrium will push such a retarded dislocation back into the array against the obstacle force (such as from a forest interaction).

collective and highly coordinate movement of partial dislocations can be driven, for example, by screw dislocation poles [46,47]. We suggest that the required highly coordinate slip of partials is the reason for the relatively unimpeded penetration of deformation twins through existing dislocation arrangements compared to an equivalent set of partial dislocations in non-coordinated motion. When one of the partials is retarded due to a forest dislocation interaction between the twin tip and the dislocation substructure in front of it, and thus deviates from its ideal position within the twin tip, the local Peach–Koehler force by the other partials assembled in the twin tip array becomes very high and pushes it back into the required dislocation configuration. For example, the force, F , on the displaced partial dislocation (displacement, x) of the twin tip depicted in Fig. 12b due to partials of the twin tip array can be considered as the force provided by two superdislocations having a magnitude Nb , where N is the number of dislocations in the twin tip array and b is the Burgers vector. Accordingly, the force F can be written as: $F/b \sim GbN/x\pi(1 - \nu) + \gamma$, where G is the shear modulus, ν is the

Poisson ratio, N is the number of dislocations in the twin tip array and γ is the stacking fault energy. Assuming a displacement x of the Burgers vector b , the force is: $F/b \sim GN/\pi(1 - \nu) + \gamma$. This force is much higher than the self-stress field of a dislocation boundary or the back-driving force created by a forest reaction product [48], and consequently the trailing partial is pushed back to its position within the twin tip.

4.2. Scaling law for dislocation cell sizes

Fig. 13 shows the variation in average size of dislocation substructures with true stress in type I and type III grains. The figure reveals that the refinement in the dislocation substructure in type III grains (HDDW structures and DCs) is less significant than that observed in type I grains (DCs). This is attributed to the activation of twinning in type III grains. As slip and twinning are two competing deformation mechanisms, the strain accommodated by slip is remarkably reduced and therefore the dislocation substructure is less refined. The figure also reveals that the variation in average size of the DCs in type I grains follows the relationship $\sigma = k/D$, where σ is the true stress, k is a constant and D is the cell size. This is a widely observed empirical relationship that has been established in the framework of the mesh-length theory of work hardening [40]. According to this theory, dislocations tend to arrange into structures which minimize the elastic energy per unit length of the dislocation line (low energy dislocation configurations). One characteristic substructure type of arrangement, viz. dislocation cell formation, minimizes the elastic energy per unit length of dislocation line through this relationship. In particular, the following relationship between the flow stress and the cell size has been proposed for cell-forming metals [40], and is known as the “similitude principle”:

$$\tau = \tau_0 + KGb/D \quad (1)$$

where τ is the flow stress, τ_0 is the friction shear stress, K is the similitude constant, G is the shear modulus, b is the Burgers vector and D is the cell size. Fig. 14 shows relation

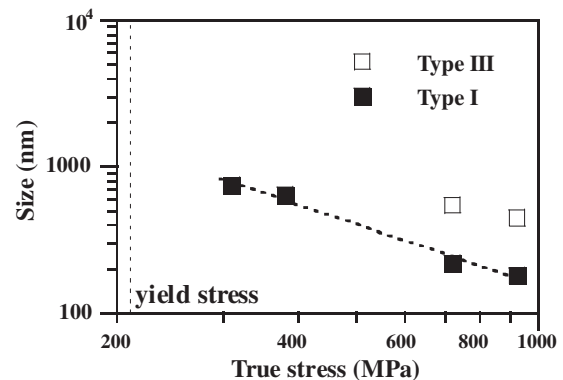


Fig. 13. Variation of the average size of the dislocation substructure with the true stress in type I grains (DCs, black symbols) and type III grains (dislocation cells plus HDDW structures, open symbols).

(1) for the present TWIP steel using $\sigma_0 = 157$ MPa [17], $b = 2.5 \times 10^{-10}$ m [15] and $G = 65$ GPa [15]. τ was obtained from σ assuming a Schmid factor m of 0.41, which corresponds to $\langle 001 \rangle // \text{TA}$ orientations. From this diagram a value for the constant K of 3.7 is obtained. This value is smaller than the commonly reported value for fcc metals (medium-to-high stacking fault energy metals), which ranges between 7 and 8 [49]. Although there are few studies on dislocation cell kinetics in low stacking fault energy alloys, a small value of the constant K between 2.0 and 2.9 has been reported for 316 L austenitic stainless steel [49,50], which is close to that obtained in the present study.

According to the mesh-length theory of work hardening, any fcc metal should develop a dislocation cell structure, according to the criterion:

$$10^2 \leq G/(\tau - \tau_0) \leq 10^5 \quad (2)$$

where G is the shear modulus, τ is the resolved shear stress and τ_0 is the friction stress. For the present steel, the term $G/(\tau - \tau_0)$ ranges between 1.7×10^2 and 1×10^3 , hence a dislocation cell structure is formed. However, it must be noted that this theory only accounts for dislocation cell formation on the basis of a low energy configuration criterion; it does not provide any detail on the kinetic mechanism of cell formation. Several observations revealed that dislocation cell formation is closely connected with the cross-slip ability of screw dislocations [48,51]. Cross-slip plays an important role in this process through the rearrangement of screw dislocations in terms of the activation of secondary slip and annihilation of screw dislocations of opposite sign. The localized maneuvers of partial dislocations to transfer dislocation screw segments from one plane to a cross-slip plane depends on the stacking fault energy [48,51]. Consequently, the stacking fault energy has an important influence on the characteristic mechanism of dislocation cell formation. For this reason, the mechanism of cell formation in the present TWIP steel may be different to that occurring in medium-to-high stacking fault energy

metals and therefore a different similitude constant K is obtained. Similar observations were recently reported in copper [49]. The material had been strained by cyclic deformation and a similar constant to that in the present study was found [49]. In their work, the authors attributed the low value of the similitude constant K to a higher storage rate of dislocations when compared to monotonic deformation. Although this aspect, viz. the high dislocation density, must also be taken into account in low stacking fault energy alloys due to the reduced activity of dislocation cross-slip, its effect on the mechanism of dislocation cell formation is not clear.

4.3. Strain hardening

Strain hardening of the Fe–22 wt.% Mn–0.6 wt.% C TWIP steel is characterized by a remarkably high strain hardening above a true stress of 270 MPa. Microstructure observations conducted by ECCI confirm that this is attributed to both dislocation accumulation and twin substructure formation.

Stage A hardening in the present alloy is characterized by a decrease in the strain hardening rate. It reveals similar features to the conventional stage III hardening regime observed in high stacking fault energy metals [28], and also agrees with previous studies on strain hardening of low stacking fault energy metals [52]. This observation suggests that this stage can be attributed to the prevalence of dynamic recovery processes, such as cross-slip and annihilation of screw dislocations of opposite signs. The microstructure observations indicate that stage B hardening, which is characterized by a constant strain hardening rate with a hardening coefficient of about $G/40$, can be attributed to the evolution of the dislocation substructure consisting of DCs and HDDW structures. The value of the strain hardening coefficient observed in this regime is much higher than the typical value of $G/200$ observed for multiple slip in common fcc metals [28] but is similar to that reported for Hadfield steels ($G/20$ – $G/30$ [33,34]). These alloys contain dislocation arrangements organized in HDDWs that act as effective obstacles against dislocation motion. Some portion of the blocked dislocations can become trapped by the boundaries, thereby increasing their dislocation density (i.e. the wall thickness). In the present alloy the presence of weaker obstacles (DCs) may result in less strain hardening. The present study hence shows for the first time the important effect of dislocation substructures on the strain hardening behavior in a TWIP steel.

The development of a dense twin substructure upon ongoing straining results in a further drastic decrease in the MFP. Consequently, strain hardening increases up to a hardening coefficient of about $G/30$, leading to stage C hardening. The microstructure observations reveal that twin boundaries cut through the existing dislocation substructure, resulting in further microstructure refinement. Twin boundaries act as strong obstacles to dislocation

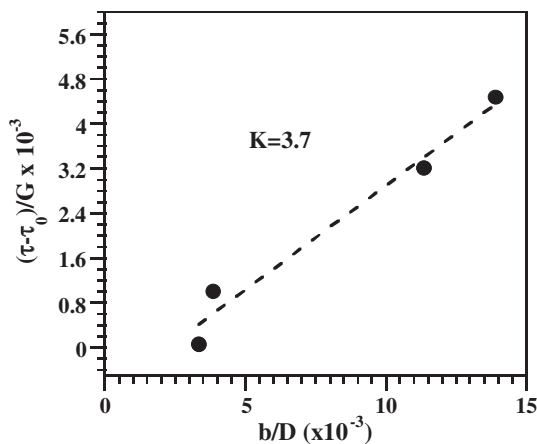


Fig. 14. Plot of the relation $(\tau - \tau_0)/G = Kb/D$ for average dislocation cell sizes in type I grains.

motion, serving as efficient sites for dislocation accumulation similar to grain boundaries. This effect is referred to as a “dynamic Hall–Petch effect”, and has been reported in many fcc metals containing deformation twins [3,15,16,52,53].

To obtain a better understanding of the influence of both dislocation and twin substructures to stage C hardening, we evaluate the contribution of the different types of grains (types I, II and III) to the flow stress at 0.3 true strain using an MFP approach. This strain level corresponds to the onset of stage D, where the highest strain hardening is obtained. The contribution of type I grains (cell forming grains) to the flow stress is provided by relation (1). Type II grains develop a block structure formed by twin boundaries and dislocation boundaries. As the average twin spacing is around half the average spacing between dislocation boundaries, we consider the average twin spacing to be the dominant microstructural correlation length in the overall MFP for mobile dislocations. Accordingly, we assume that the contribution of type II grains to the flow stress can be described in terms of a Hall–Petch-type relation [52]:

$$\sigma = \sigma_0 + K_{H-P}/(\lambda_{\text{twin}})^{1/2} \quad (3)$$

where σ_0 is the friction stress, K_{H-P} is the Hall–Petch constant for twinning and λ_{twin} is the average twin spacing. Type III grains develop a block structure formed by twin and dislocation boundaries (HDDWs and cell walls). As a first approximation, we consider only the smallest obstacle spacing, which is the average twin spacing of one of the active twinning system. We therefore assume that the contribution of type III grains to the flow stress is also provided by relation (3), with λ_{twin} being the smallest average twin spacing of the active twin system. Considering these three contributions, the expression for the flow stress can be written as:

$$\sigma = \sigma_0 + f_I G K b M / D + f_{II} K_{H-P} / (\lambda_{\text{twin}}^{II})^{1/2} + f_{III} K_{H-P} / (\lambda_{\text{twin}}^{III})^{1/2} \quad (4)$$

where σ_0 is the friction stress, f_I , f_{II} and f_{III} are the area fractions of type I, II and III grains, respectively, G is the shear modulus, b is the Burgers vector, K is a constant, M is the Taylor factor, D is the average cell size, K_{H-P} is the Hall–Petch constant for twinning, $\lambda_{\text{twin}}^{II}$ is the average twin spacing in type II grains, and $\lambda_{\text{twin}}^{III}$ is the smallest average twin spacing of an active twin system in type III grains. The area fraction, average size of dislocation substructures and average twin spacing of each type of grain are shown in Table 1. Assuming $\sigma_0 = 157$ MPa [17], $b = 2.5 \times 10^{-10}$ m [15], $G = 65$ GPa [15], $K = 3.7$ (calculated in the previous section), $M = 2.44$ (Taylor factor for type I grains) and $K_{H-P} = 357$ MPa $\mu\text{m}^{1/2}$ [17] (a previous work has shown that in the present TWIP steel the Hall–Petch constant for twinning is similar to that for slip [6]), and taking the microstructure parameters shown in Table 1, yields a flow

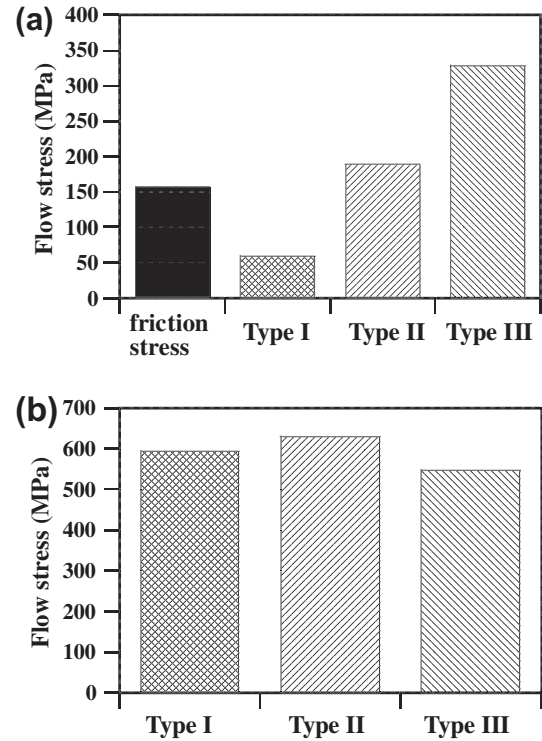


Fig. 15. (a) Contribution of the friction stress and type I, II and III grains to the flow stress at 0.3 true strain. (b) Intrinsic strength of type I, II and type III grains at 0.3 true strain. Type I grains: equiaxed cell structure with a low deformation twinning activity; type II grains: well-developed twin substructure along one active twinning system (primary twin system); type III grains: DCs and HDDW structures with a well-developed twin substructure along more than one active twinning system (primary and secondary twin systems) (see also Fig. 7 and Table 1).

stress of 735 MPa at 0.3 true strain. This value is close to the experimentally observed flow stress value of 720 MPa.

Two important findings can be drawn from this estimate. First, the strain hardening of a TWIP steel can be analyzed in terms of the MFP approach. This result agrees with published models on the hardening behavior of TWIP steels [13,14,17]. Second, we have identified the different microstructure parameters controlling strain hardening in this material, namely, the average dislocation cell size in type I grains, the average twin spacing in type II grains and the smallest average twin spacing of the active twin system in type III grains. Fig. 15a shows the contribution to the flow stress of each term occurring in relation (4). The figure reveals that the most significant contribution to the flow stress is provided by the twin substructure (type II and III grains) with about 70% contribution to the overall flow stress. In particular, type III crystals, which are the most frequently occurring grains, provide the highest contribution. Interestingly, the contribution of the dislocation substructure, which is mainly provided by type I grains, is still noticeable, with about 8% of the flow stress. This analysis clarifies the influence of the main microstructure features, namely dislocation and twin substructures, on the high strain hardening rate of TWIP steels. It shows that the high strain hardening rate observed in stage C is mainly attributed to the MFP refinement due to deformation

twinning in type II and III grains. If we only consider the intrinsic strength of each type of grain, we find that type II crystals (with a lamellar twin structure) are the hardest grains (Fig. 15b). Interestingly, this figure reveals that at this deformation stage type I grains (cell forming grains) exhibit an even higher strength than type III grains (multiple twin structure). This result supports the previous finding of the significant contribution of dislocation substructures on strain hardening in the present TWIP steel.

With further straining, the refinement of the twin spacing proceeds, leading to a further reduction in the dislocation MFP and a gradual decrease in the strain hardening rate. The hardening coefficient of stage D is still high ($G/30$), indicating the gradual refinement of the MFP, as also revealed by Table 1. Above a true stress of 800 MPa, in stage E, strain hardening steadily decreases, indicating the reduced capability for trapping more dislocations inside the refined microstructure. The work hardening capability is determined not only by the MFP but also by the specific strengthening effect of the deformation twins when they act as obstacles against dislocation motion. In the present FeMn alloy, deformation twins are arranged in bundles. Microstructure observations reveal that the bundle density and thickness increase gradually with strain. This indicates that the number of deformation twins arranged in bundles increases with the strain as well. These bundles are even stronger obstacles to dislocation glide than single twins because the critical stress required to carry plastic deformation across the twin bundle is much higher than that required to penetrate a single twin due to the small interface spacing. Another result supporting the increasing twin strength with deformation is the high density of sessile dislocations found within twin lamellae in an Fe–20 wt.% Mn–1.2 wt.% C TWIP steel [7,18]. The accumulation of sessile dislocations within the twin is attributed to dislocation reactions between Shockley partials and twin dislocations. These sessile dislocations are potential obstacles to dislocation motion and can provide not only a hardening mechanism within deformation twins but also an increase in the critical stress required to induce plastic deformation across the twin as well. Furthermore, in the present TWIP steel, Shockley partial-twin dislocation interactions can be enhanced by the interaction between HDDWs and cell boundaries with twin boundaries. Accordingly, we suggest that, in the present TWIP steel, deformation twins contain a high dislocation density as well. As the dislocation density is increased by dislocation storage through interactions, the dislocation density will increase with further deformation. These two aspects associated with the role of deformation twins, namely the arrangement in twin bundles and the high dislocation density within them, increase the stress required to transfer plastic deformation across deformation twins and therefore limit the further work hardening capacity at high strains in this material.

5. Conclusions

We have investigated the underlying defect topology and kinetics of substructure evolution and its correspondence to the strain hardening evolution of an Fe–22 wt.% Mn–0.6 wt.% C TWIP steel during tensile deformation by means of ECCI and EBSD. We draw the following conclusions:

- At the early stages of plastic deformation (below 0.1 true strain), the microstructure consists of dislocation cells and highly dense dislocation arrangements. These dislocation substructures are strong barriers to dislocation glide and result in a high strain hardening with a hardening coefficient of about $G/40$. This result underlines the importance of dislocation substructures at the early stages of strain hardening in TWIP steels.
- At intermediate strains (0.1–0.3 true strain), a well-defined deformation twin substructure is developed. Twinning depends on the crystallographic grain orientation. We classify the microstructure in this regime according to its twin substructure into three groups, referred to as types I, II and III. We quantify strain hardening in terms of a dislocation mean free path approach. The different microstructure parameters controlling strain hardening in this regime are: the average dislocation cell size in type I grains; the average twin spacing in type II grains; and the smallest average twin spacing of an active twin system in type III grains. The analysis shows that the refinement in the dislocation mean free path due to deformation twinning in type II and III grains results in a high strain rate with a hardening coefficient of about $G/30$.
- At high strains (above 0.4 true strain), the reduced further refinement of the dislocation and twin substructure together with the increasing strengthening effect of the individual deformation twins as obstacles to dislocation glide reduce the capability for trapping more dislocations, hence the strain hardening decreases.
- The cell structure formed in type I grains follows the similitude principle $\tau = \tau_0 + KGb/D$ with a similitude constant of $K = 3.7$. This value is smaller than the value of 7–8 that is typically observed in medium-to-high stacking fault alloys. We attribute this difference to the influence of the stacking fault energy on the mechanism of cell formation.

Acknowledgements

The authors would like to acknowledge the financial support by the German Research Foundation (Deutsche Forschungsgemeinschaft DFG) within the framework of the SFB 761 “steel ab initio”.

References

- [1] Grässel O, Krüger L, Frommeyer G, Meyer LW. *Int J Plast* 2000;16:1391.
- [2] Lü Y, Hutchinson B, Molodov DA, Gottstein G. *Acta Mater* 2010;58:3079.
- [3] Jin JE, Lee YK. *Mater Sci Eng A* 2009;527:157.
- [4] Kim JK, Chen L, Kim HS, Kim SK, Estrin Y, Cooman BCD. *Metall Mater Trans A* 2009;40:3147.
- [5] Curtze S, Kuokkala VT. *Acta Mater* 2010;58:5129.
- [6] Gutierrez-Urrutia I, Zaeferrer S, Raabe D. *Mater Sci Eng A* 2010;527:3552.
- [7] Idrissi H, Renard K, Schryvers D, Jacques PJ. *Scripta Mater* 2010;63:961.
- [8] Lü Y, Molodov DA, Gottstein G. *Acta Mater* 2011;59:3229.
- [9] Yoo JD, Park KT. *Mater Sci Eng A* 2008;496:417.
- [10] Yoo JD, Hwang SW, Park KT. *Metall Mater Trans A* 2009;40:1520.
- [11] Olson GB, Cohen M. *Metall Trans A* 1976;7:1897.
- [12] Olson GB, Cohen M. *Metall Trans A* 1976;7:1905.
- [13] Allain S, Chateau JP, Bouaziz O. *Mater Sci Eng A* 2004;387–389:143.
- [14] Shiekhelesouk MN, Favier V, Inal K, Cherkaoui M. *Int J Plast* 2009;25:105.
- [15] Bouaziz O, Allain S, Scott C. *Scripta Mater* 2008;58:484.
- [16] Barbier D, Gey N, Allain S, Bozzolo N, Humbert M. *Mater Sci Eng A* 2009;500:196.
- [17] Sevillano JG. *Scripta Mater* 2009;60:336.
- [18] Idrissi H, Renard K, Ryelandt L, Schryvers D, Jacques PJ. *Acta Mater* 2010;58:2464.
- [19] Ng BC, Simkin BA, Crimp MA. *Mater Sci Eng A* 1997;239–240:150.
- [20] Wilkinson AJ, Hirsch PB. *Micron* 1997;28:279.
- [21] Ng BC, Simkin BA, Crimp MA. *Ultramicroscopy* 1998;75:137.
- [22] Ahmed J, Roberts SG, Wilkinson AJ. *Philos Mag* 2006;86:4965.
- [23] Crimp MA. *Microsc Res Tech* 2006;69:374.
- [24] Gutierrez-Urrutia I, Zaeferrer S, Raabe D. *Scripta Mater* 2009;61:737.
- [25] Weidner A, Martin S, Klemm V, Martin U, Biermann H. *Scripta Mater* 2011;64:513.
- [26] Senk D, Emmerich H, Rezende J, Siquieri R. *Adv Eng Mater* 2007;9:695.
- [27] Raabe D, Sachtleber M, Zhao Z, Roters F, Zaeferrer S. *Acta Mater* 2001;49:3433.
- [28] Kocks UF, Mecking H. *Prog Mater Sci* 2003;48:171.
- [29] Ueji R, Tsuchida N, Terada D, Tsuji N, Tanaka Y, Takemura A, et al. *Scripta Mater* 2008;59:963.
- [30] Bay B, Hansen N, Hughes DA, Kuhlmann-Wilsdorf D. *Acta Metall Mater* 1992;40:205.
- [31] Hansen N. *Scripta Metall Mater* 1992;27:1447.
- [32] Hansen N, Jensen DJ. *Philos Trans Roy Soc* 1999;357:1447.
- [33] Canadinc D, Sehitoglu H, Maier HJ, Chumlyakov YI. *Acta Mater* 2005;53:1831.
- [34] Canadinc D, Sehitoglu H, Maier HJ. *Mater Sci Eng A* 2007;454–455:662.
- [35] Gerold V, Karnthaler HP. *Acta Metall* 1989;37:2177.
- [36] Hong SI, Laird C. *Acta Metall Mater* 1990;38:1581.
- [37] Kassner ME, Miller AK, Sherby OD. *Metall Trans A* 1982;13:1977.
- [38] Lo KH, Shek CH, Lai JKL. *Mater Sci Eng R* 2009;65:39.
- [39] Bracke L, Kestens L, Penning J. *Scripta Mater* 2009;61:220.
- [40] Kuhlmann-Wilsdorf D. *Mater Sci Eng A* 1989;113:1.
- [41] Hansen N, Huang X. *Acta Mater* 1998;46:1827.
- [42] Winther G, Jensen DJ, Hansen N. *Acta Mater* 1997;45:5059.
- [43] Mitchell TE, Hirth JP. *Acta Metall Mater* 1991;39:1711.
- [44] Kamat SV, Hirth JP, Müllner P. *Philos Mag A* 1996;73:669.
- [45] Müllner P, Solenthaler C, Speidel MO. *Acta Metall Mater* 1994;42:1727.
- [46] Christian JW, Mahajan S. *Prog Mater Sci* 1995;39:1.
- [47] Niewczas M. In: Nabarro FRN, Hirth JP, editors. *Dislocations in solids*, vol. 13. Amsterdam: Elsevier B.V.; 2007.
- [48] Hirth JP, Lothe J. *Theory of dislocations*. 2nd ed. New York: John Wiley and Sons; 1982.
- [49] Sauzay M, Kubin LP. *Prog Mater Sci* 2011;56:725.
- [50] Feaugas X. *Acta Mater* 1999;47:3617.
- [51] Jackson PJ. *Prog Mater Sci* 1985;29:139.
- [52] Asgari S, El-Danaf E, Kalidindi SR, Doherty RD. *Metall Mater Trans A* 1997;28:1781.
- [53] Karaman I, Sehitoglu H, Maier HJ, Chumlyakov YI. *Acta Mater* 2001;49:3919.